# Journal Pre-proof

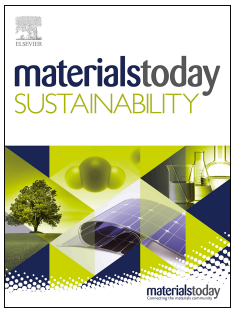


Development of Sustainable Mixed Recycled Wrought Aluminium Alloys with Modified $Al_3(Sc,Ti)$ for Improved Impurity Tolerance

Zhongping Que, Raluca Florentina Negrea, Changming Fang

PII: S2589-2347(26)00096-5

DOI: https://doi.org/10.1016/j.mtsust.2026.101395

Reference: MTSUST 101395

To appear in: *Materials Today Sustainability*

Received Date: 16 March 2026

Revised Date: 19 May 2026

Accepted Date: 21 May 2026

Please cite this article as: Z. Que, R.F. Negrea, C. Fang, Development of Sustainable Mixed Recycled Wrought Aluminium Alloys with Modified $Al_3(Sc,Ti)$ for Improved Impurity Tolerance, *Materials Today Sustainability*, https://doi.org/10.1016/j.mtsust.2026.101395.

# Graphical Abstract

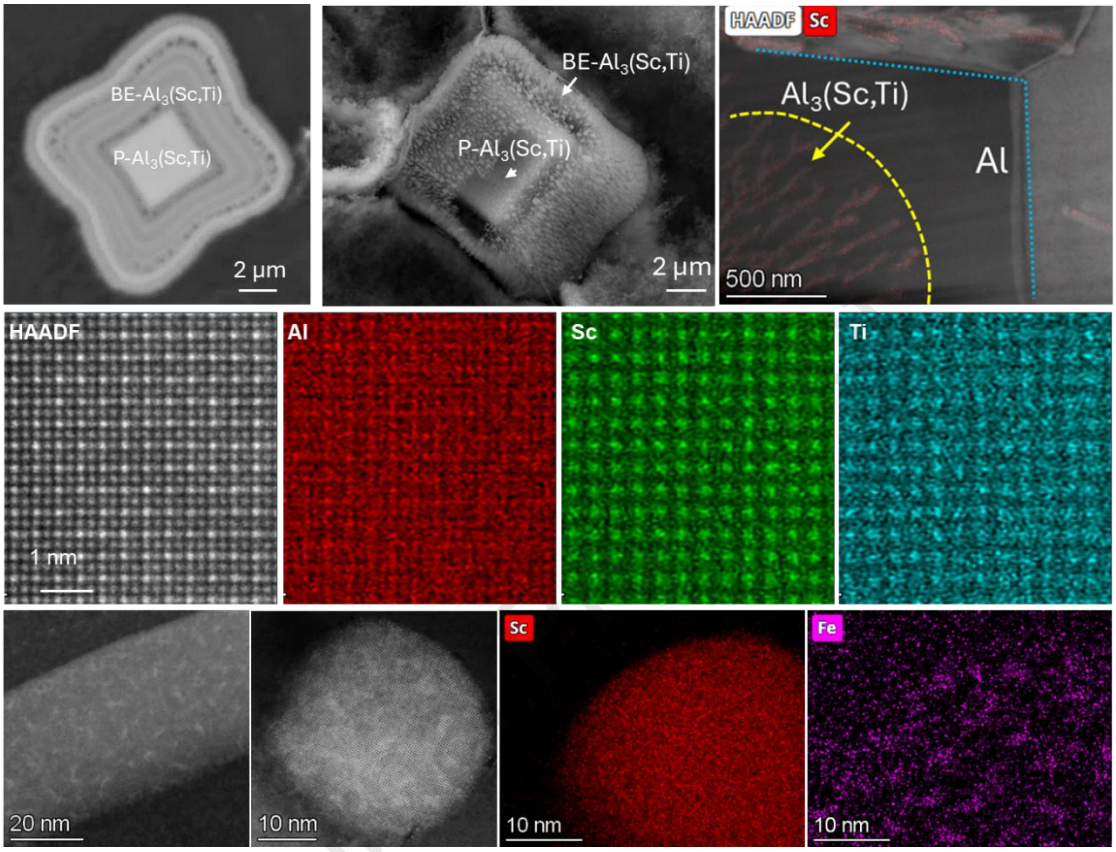

# Development of Sustainable Mixed Recycled Wrought Aluminium Alloys with Modified $Al_3(Sc,Ti)$ for Improved Impurity Tolerance

Zhongping Que*, Raluca Florentina Negrea, Changming Fang

Brunel Centre for Advanced Solidification Technology (BCAST), Brunel University London, Uxbridge, Middlesex UB8 3PH, UK

*Corresponding author. E-mail address: Zhongping.Que@brunel.ac.uk

**Abstract:**

A representative cross-recycled wrought aluminium alloy, Al–1.33Si–1.28Mg–0.97Cu–0.88Zn–0.51Fe–0.57Mn–0.14Cr–0.09Ti (wt.%), was designed based on mixed 1xxx–7xxx series compositions with maximised impurity levels to emulate realistic recycling streams. To enhance impurity tolerance and microstructural stability in such complex recycled alloys, the role of scandium (Sc) was systematically investigated. While Sc is widely recognised in aluminium alloys for grain refinement via primary $Al_3Sc$ particles and precipitation strengthening through coherent nanoscale $Al_3Sc$ dispersoids, its behaviour in recycled aluminium systems remains largely unexplored. Here, we examine the formation, morphology, composition, crystallography, and impurity tolerance, particularly with respect to Fe and Si, of $Al_3(Sc,Ti)$ in this cross-recycled alloy. Competitive formation of primary $Al_3(Sc,Ti)$ and eutectic ($Al_3(Sc,Ti)$ + α-Al) is observed. Combined experimental characterisation and density functional theory calculations reveal preferential substitution of Ti for Sc in the $L1_2$ lattice, reducing the lattice misfit with α-Al to nearly zero and promoting heterogeneous nucleation. $Al_3(Sc,Ti)$ exhibits remarkable tolerance to a broad range of impurities, with Fe, Mn, Cr, Si, Cu, Mg, Ti and Zn accommodated through defect-mediated incorporation and local chemical interactions at elevated temperatures. Atomic-resolution STEM further reveals Fe clusters embedded within as-cast $Al_3(Sc,Ti)$ particles, while heat treatment induces surface segregation of major alloying elements, indicating dynamic solute redistribution. These results establish the intrinsic impurity tolerance of $Al_3(Sc,Ti)$ and provide mechanistic insight into solute partitioning and phase stability in complex recycled aluminium alloys, offering guidance for the design of sustainable, high-performance aluminium systems from mixed recycled feedstocks.

**Key words:** $Al_3(Sc,Ti)$, Impurity tolerance, Recycled Al alloys, STEM–EDS characterization, Fe cluster

## 1. Introduction

Addressing the urgent global challenge of decoupling economic growth from environmental degradation, requires more holistic approaches to sustainable manufacturing where metals playing a critical role [1]. Aluminium (Al) stands out due to its strength, low weight, and exceptional recyclability [2-3]. However, the current Al sector remains heavily dependent on energy-intensive primary production, which is environmentally unsustainable and risks undermining net-zero ambitions [4-5]. Unlocking Al's full circular potential through advanced

recycling is vital to reducing carbon emissions, conserving resources, and securing supply chains worldwide. The transition to high-quality secondary Al, however, is constrained by persistent technical barriers, particularly the challenge of managing impurities and non-metallic inclusions in scrap. These issues lead to downcycling, where the properties of recycled alloys are degraded [6-7]. Contaminants such as organic oils, mixed alloy grades, and other inclusions, often carried over from diverse scrap sources, compromise the mechanical integrity and reliability of recycled aluminium. This challenge is particularly pronounced in high-performance Al alloys, where meeting both sustainability goals and strict structural integrity requirements in recycled alloys remains difficult [6, 8-9].

Microstructure refinement, typically through grain refinement, is a common strategy to reduce casting defects and thereby enhance the performance of recycled aluminium alloys [10]. Combining grain refinement with fine precipitates has become a conventional approach in solidification technologies to produce high-performance Al alloys that meet strict mechanical and structural requirements [11]. In this context, Scandium (Sc) plays a critical role [12-20]. Even in small additions (typically 0.1–0.5 wt%), Sc forms fine, coherent $Al_3Sc$ precipitates that significantly strengthen the alloy through precipitation hardening. These precipitates impede dislocation motion, improving yield strength, tensile strength, and creep resistance, while simultaneously refining the grain structure and limiting grain growth during processing [14-18]. Furthermore, Sc additions enhance weldability and corrosion resistance, making Al–Sc alloys highly attractive for aerospace, automotive, and sporting applications where a combination of low density, high strength, and durability is required [19-20].

Investigations into the influence of alloying elements on $Al_3Sc$ formation have mainly focused on nanoscale $Al_3Sc$ dispersoids formed during solid-state precipitation. Previous studies have shown that several alloying elements, such as Si, Zr, Ti, and Hf, exhibit varying degrees of solubility in $Al_3Sc$ [21-25]. For example, Si has been reported to substitute at Al sites, leading to the formation of modified $(Al,Si)_3Sc$ phases [21], while higher Si concentrations may further promote the formation of Al–Sc–Si intermetallic compounds [26]. In contrast, elements such as Zr, Ti, and Hf preferentially occupy the Sc sublattice sites. These alloying additions can significantly influence the formation kinetics, thermal stability, and coarsening resistance of $Al_3Sc$ precipitates, particularly during heat treatment and ageing processes. Consequently, most previous studies have concentrated on precipitation behaviour and microstructural evolution under post-solidification conditions. In comparison, the direct interaction between typical tramp elements, such as Fe, Mn, and Cr, and $Al_3Sc$ remains much less understood, especially in complex recycled Al alloys. This lack of understanding is becoming increasingly important due to the growing demand for sustainable and recycled Al alloys, where impurity accumulation is one of the major barriers limiting alloy upcycling and property control.

Due to the high cost of Sc, most previous research has focused on relatively low Sc additions (~0.1–0.6 wt.%) to optimise precipitation strengthening, grain refinement, and thermal stability while maintaining economic feasibility. As a result, investigations of higher Sc additions and the formation behaviour of primary $Al_3Sc$ phases during solidification have remained comparatively limited. The potential benefits of primary $Al_3Sc$ formation, particularly in relation to impurity tolerance and solidification control in recycled alloys, therefore, remain largely unexplored. In recent years, our research group has focused on the development of

sustainable Al alloys through advanced solidification technologies and systematic investigations into the role of Sc in recycled multicomponent Al alloys. Several novel phenomena have been identified using characterisation techniques spanning from casting-scale analysis to atomic-resolution microscopy. For example, at relatively low Sc additions, a unique grain refinement mechanism involving twinned eutectic ($Al_3$(Sc,Ti)+Al) cells [27] was discovered, which not only physically restricts α-Al growth during solidification but also introduces additional internal boundaries that contribute to improved mechanical performance. However, with higher Sc additions leading to the formation of primary $Al_3Sc$ particles (e.g., ~1.0 wt.% Sc), a unique high-angle grain boundary structure was discovered on individual $Al_3$(Sc,Ti) particles, which provided an almost zero lattice misfit with α-Al [28]. These multiple grain boundaries not only provide significantly enhanced grain refinement efficiency for α-Al, but also contribute to improved impurity tolerance in recycled Al alloys.

Building on these findings, the present study reports, for the first time, the elemental interaction between multiple impurity/alloying elements (Cu, Si, Mg, Zn, Fe, Mn, Ti, and Cr) and primary $Al_3$(Sc,Ti) particles in complex recycled Al alloys. This work reveals previously unreported impurity redistribution and clustering behaviour associated with $Al_3$(Sc,Ti) during solidification and heat treatment. More importantly, it provides new insight into impurity tolerance mechanisms in recycled Al alloys, which is currently a critical but insufficiently understood issue for the future upcycling and sustainable development of high-performance aluminium alloys.

In this study, the interaction between $Al_3Sc$ and impurities in cross-recycled wrought aluminium alloys is systematically investigated. The study identifies which impurity elements can be incorporated into $Al_3Sc$ and examines their influence on its crystal structure and morphology. Notably, Fe, which has previously been reported as energetically unfavourable within $Al_3Sc$, was observed to form clusters inside $Al_3Sc$ particles, indicating an unexpected impurity tolerance of the phase. Detailed TEM and STEM analyses reveal that, regardless of whether $Al_3Sc$ forms as primary particles during solidification or as static dispersoid precipitates in the eutectic ($Al_3Sc$ + α-Al) region, both types of $Al_3Sc$ particles can effectively interaction with the impurities within the recycled Al alloys and how these impurities effect the lattice parameters of the $Al_3Sc$.

In this study, a cross-recycled wrought aluminium alloy, Al-1.33Si-1.28Mg-0.97Cu-0.88Zn-0.51Fe-0.57Mn-0.14Cr-0.09Ti (wt.%), was designed to represent a realistic recycled composition containing most of the major (≤1.0 wt.%) and minor (0.1-1.0 wt.%) alloying elements commonly found in commercial wrought Al series [29]. The alloying elements in each selected grade were chosen at their upper permissible limits, representing a case containing the maximum level of impurities. This alloy was employed to systematically investigate the impurity effects on the formation of $Al_3Sc$ and to assess the influence of Sc on secondary phase formation within a complex recycled aluminium matrix. The morphology, size, and size distribution of $Al_3Sc$ particles, as well as the crystallographic variations induced by impurity incorporation, were examined in detail. The solidification sequence competition between primary $Al_3Sc$ and the eutectic ($Al_3Sc$ + α-Al) reaction was analysed to elucidate their respective roles in grain refinement.

## 2. Experimental

### *2.1 Alloy Design*

The study introduces a new design strategy for wrought Al by leveraging the impurities present in cross-over RA, spanning the 1xxx to 7xxx series. These alloys contain a variety of alloying elements, including major elements (>1 wt.%), minor elements (0.1 wt.% < x < 1.0 wt.%), and trace elements (<0.1 wt.%). One representative alloy with most industrial application from each series was selected (A1050, A2024, A3003, A4043, A5052, A6082, A7075) as listed in Table 1, and assumed to be equally mixed. All major and minor alloying elements were considered as constituent elements. The upper compositional limits of each selected alloy were used to formulate the RA, which resulting in a composition of: 1.34 wt.% Si, 1.31 wt.% Mg, 1.09 wt.% Cu, 1.00 wt.% Zn, 0.56 wt.% Fe, 0.58 wt.% Mn, 0.13 wt.% Cr, and 0.09 wt.% Ti, with the balance of Al, Table 2. This RA contains a significantly higher total concentration of alloying elements (6.0 wt.%) compared to commercial alloys, such as A6082 (~2.48 wt.%).

### *2.2 Casting*

The alloy was produced using commercial-purity (CP) aluminium (99.9%), CP magnesium (>99.95%), CP zinc (>99.95%), and several master alloys: Al-50%Si, Al-20%Mn, Al-10%Ti, Al-20%Cr, and Al-38%Fe. To compensate for potential losses of volatile elements such as magnesium during melting, an additional 3% CP-Mg was added to the melt, ensuring that the final composition closely matched the nominal target. The Al-2%Sc master alloy was used for scandium additions. The prepared Al alloys contain composition as 1.34 wt.% Si, 1.31 wt.% Mg, 1.09 wt.% Cu, 1.00 wt.% Zn, 0.56 wt.% Fe, 0.58 wt.% Mn, 0.13 wt.% Cr, and 0.09 wt.% Ti, with the balance being aluminium, as shown in Table 2.

The CP-Al and all the master alloys were first melted at 800 ℃ in an electric resistance furnace, followed by thorough stirring to ensure complete dissolution. CP-Mg and CP-Zn were wrapped in Al foil, preheated to 200 ℃, and then introduced into the melt. After complete melting of the Mg and Zn, the melt was held for an additional 30 minutes.

Following slag removal, the molten alloys, with and without 1.0% Sc addition were cast into two types of moulds: a Tp-1 mould [30] for microstructure investigation. The Tp-1 mould is specifically designed to provide a cooling rate of 3.5 K/s at a point 38 mm from the bottom of the casting, replicating conditions of industrial direct chill (DC) casting. The Tp-1 mould was preheated to 380 ℃, and the alloys were poured at a temperature of 750 ℃. The phase diagram of the RA alloy was calculated using the Scheil model [31] in Pandat software, and the experimental cooling rate was measured with an IDECO machine.

### *2.3 Characterization*

Metallographic specimens were prepared using standard procedures. The as-cast microstructures were examined using a Zeiss optical microscope equipped with AxioVision 4.3 image analysis software. Scanning electron microscopy (SEM) analyses were conducted using a Zeiss Crossbeam 340 FIB-SEM operated at an accelerating voltage of 20 kV. To reveal the three-dimensional (3D) morphology of the Sc-containing intermetallic compounds (Sc-IMCs),

the Tp-1 samples were deep-etched in a 20 vol.% HCl aqueous solution for approximately 5 minutes, followed by cleaning in an ethanol bath and thorough drying.

TEM specimens were prepared by two routes. Site-specific lamellae containing primary $Al_3Sc$ particles were fabricated by focused ion beam (FIB) milling using a Zeiss Crossbeam 340 FIB-SEM due to the difficulty of extracting these particles by conventional methods. Additional TEM foils were prepared by mechanical grinding to ~60 μm thickness, followed by final thinning using a precision ion polishing system (PIPS) with voltage of 1-5kv with angle of 1-7°. STEM-EDS analyses were performed on multiple FIB- and PIPS-prepared TEM samples. The FIB-prepared samples showed relatively higher Cu quantification due to the influence of the Cu sample grid material. However, because of the difficulty in preparing TEM samples containing primary $Al_3(Sc,Ti)$ particles, the FIB technique has to be employed.

TEM observations were carried out using a $C_s$-corrected SPECTRA 300 TEM (Thermo Fisher Scientific), equipped with a Super-X EDS detector and operated at an accelerating voltage of 200 kV. The crystal structure modelling, HAADF - STEM image simulations, and heterogeneous nucleation behaviour between the $Al_3(Sc_{1-x}Ti_x)$ phase and the α-Al matrix were investigated using *CrystalMaker* version 10.0, *CrystalKit* and *Tempas* software (Total Resolution LLC). It should be noted that the STEM results presented in this work are based on systematic investigations of multiple particles rather than a single individual particle.

A plane-wave approach implanted in the first-principles Vienna Ab initio Simulation Package [32] was employed in the present study. The generalized gradient approximation (PBE-GGA) [33] within the projector-augmented wave frame [34] was used for the correlation and exchange terms. High cut-off energies (ECUT/EAUG=400.0 eV/550.0 eV) were set for the present calculations. Dense k-meshes for the structural optimizations and total energy calculations were used, e.g., a 10×10×10 mesh with k-points ranging from 35 to 250 for the L12-phase supercells, depending on the symmetry in the Brillouin zone on the Monkhorst-Pack approach [35]. Test calculations for the cut-off energies and k-meshes produced results of high reliability and accuracy with energy deviations within 1meV/atom.

## 3. Results

### *3.1 Formation of primary $Al_3(Sc,Ti)$ particles*

Figure 1 shows the as-cast microstructure of studied recycled Al alloy solidified at 3.5K/s without and with addition of 1.0wt.% Sc. Figure 1a shows that the RA alloy cast at a cooling rate of 3.5 K/s exhibits a typical wrought Al alloy microstructure, consisting α-Al grains, second-phase particles (SPPs), including Al-rich Fe-intermetallic compounds (IMCs), $Mg_2Si$ and Cu-rich IMCs, are located along the grain boundaries. No primary intermetallic compounds were detected in the microstructure. Figure 1b show that after addition of 1.0 wt.% Sc, obvious cubic like Sc-rich particles which were identified as $Al_3(Sc,Ti)$ particles later were observed within the Al gains. The average of these $Al_3(Sc,Ti)$ particle sizes is 10 ±1.2μm. Nearly every grain contained at least one Sc-IMC under random examination, suggesting strong nucleation potency for α-Al. A comprehensive analysis of these results will be reported in a subsequent publication. the types of SPPs at the grain boundary remains unchanged, except for a notable reduction in Cu-rich multicomponent eutectic droplets, indicating a change in solubility after

Sc addition. Figure 1 also demonstrates the typical influence of grain refinement on the distribution of second-phase particles (SPPs) at the grain boundaries. Figure 1a shows a relatively high number density but finer size of Fe-containing intermetallic compounds (Fe-IMCs) distributed along the grain boundaries in the recycled alloy without Sc addition. In contrast, Fig. 1b shows a significantly lower number density of Fe-IMCs after grain refinement induced by Sc addition, although the remaining Fe-IMCs appear relatively coarser. Quantitative analysis of the 2D image area fraction indicates that the recycled alloy without grain refinement contains approximately 3.7 ± 0.3% Fe-IMCs, whereas the grain-refined alloy with 1.0 wt.% Sc contains approximately 3.4 ± 0.3% Fe-IMCs. These results suggest the volume fraction of Fe-IMCs are at the equivalent level, and that Sc-induced grain refinement might slightly reduce the overall fraction of Fe-IMCs while simultaneously modifying their distribution and morphology which will be introduced in later sections. Investigation of the $Al_3$(Sc,Ti) particle morphology revealed a complex relationship between particle shape and the surrounding microstructure. Figure 2a shows an SEM-BSD image of an $Al_3$(Sc,Ti) particle consisting of a solid central cubic core surrounded by a ring-like region containing two phases. This region transitions from well-defined cubic edges to curved surfaces with a dendritic morphology.

Deep etching exposed the 3D morphology of these particles, revealing a fluffy, fibre-like surface composed of a eutectic mixture of $Al_3$(Sc,Ti) and α-Al. Figure 2c shows that deeper etching exposes the solid cubic core more clearly. High-magnification SEM images (Figures 2d and 2e) demonstrate that both the eutectic phase and the secondary $Al_3$(Sc,Ti) structures grow outward from the central primary $Al_3$(Sc,Ti) cube.

Because the $Al_3$(Sc,Ti) + α-Al eutectic structure has a much faster etching rate than the central $Al_3$(Sc,Ti) core, the eutectic shell surrounding the primary $Al_3$(Sc,Ti) particles can be partially or completely removed during deep etching. This allows the morphology of the primary $Al_3$(Sc,Ti) particles to be revealed more clearly.

Figure 3 presents several examples of these morphological variations, along with corresponding schematic diagrams illustrating the transition in particle shape. The primary $Al_3$(Sc,Ti) particles may appear as solid cubic (Figure 3a), or as cubic with face-centred, elongated cavities. The morphology of these cavities evolves from square (Figure 3b) to circular (Figure 3e), eventually leading to a slightly depressed face surface (Figure 3f). Twinning features along the 45° {100} directions can also be observed (Figure 3c).

### *3.2 Identification of $Al_3$(Sc,Ti)*

These featured $Al_3$(Sc,Ti) particles covered with $Al_3$(Sc,Ti) + α-Al eutectic shells were analysed with SEM-EDS mapping, Figure 4 a. It shows that both the central primary $Al_3$(Sc,Ti) and the $Al_3$(Sc,Ti) within the eutectic shells are rich with Sc and Ti. Further STEM investigation reveals that the outer eutectic shell are consisted with $Al_3$(Sc,Ti) with dendritic morphology and the rest of α-Al, Figure 4b and 4d. STEM-HAADF investigation confirmed that multiple orientation existing within one $Al_3$(Sc,Ti) particle and the transition layers within the BE and actually connected by growth from one of the orientations. Figure 4d shows that although the

BE-($Al_3$(Sc,Ti) + α-Al) surface looks curved under SEM, it actually terminated with cubic faceted. Further atomic resolution HAADF image and atomic resolution STEM-EDS mapping in Figure 4d reveals the elemental distribution inside the Al-Sc-Ti particle. The concentration of Ti is much lower than that of Sc and also incorporate at the Sc atomic sites. The measured composition of this primary Sc phase is list in Table 3, as 20.96 ± 1.68 wt.% Sc, 5.13± 0.57 wt.% Ti, 0.87 ± 0.19 wt.% Si, 0.07 ± 0.02 wt.% Mn, 0.09 ± 0.02 wt.% Fe, 4.24 ± 0.45 at.% Cu, 0.07 ± 0.02 wt.% Mg, and 0.54 ± 0.04 wt.% Zn. Or 14.58± 2.8 at.% Sc, 3.34± 0.76 at.% Ti, 0.96 ± 0.24 at.% Si, 0.04 ± 0.01 at.% Mn, 0.05 ± 0.01 at.% Fe, 2.08 ± 0.45 at.% Cu, 0.09 ± 0.02 at.% Mg, and 0.26 ± 0.05 at.% Zn, corresponding to an Al/(Sc+Ti) atomic ratio of 3.76. This ratio is lower than 3:1 but approaches 4:1. The deviation in the atomic ratio may result from the incorporation of other impurities, such as Si, Cu, Mg, and Zn, which can potentially occupy the Al lattice sites. In addition, the weight percentage of Cu is approximately 4.2%, which is unavoidably caused by the FIB sample grid which produced with Cu material.

The Ti concentration in the primary $Al_3Sc$ particles that solidified at higher temperatures is significantly higher than that in the $Al_3Sc$ precipitates formed during the later stages of solidification, because the primary particles form earlier from the liquid phase. Other impurities, such as Fe, Mn, and Si, could also potentially be trapped at higher concentrations in the primary $Al_3Sc$ particles compared with the later $Al_3Sc$ precipitates. However, the larger driving force resulting from the higher solute concentration, elevated formation temperature, and energetically unfavourable solid solution state promotes the precipitation of Fe-containing intermetallic compounds (Fe-IMCs) within the primary $Al_3Sc$ particles. Consequently, the concentrations of these tramp elements are reduced. In contrast, the driving force for Fe-IMC precipitation in the later $Al_3Sc$ precipitates is much lower due to the lower formation temperature; therefore, Fe clusters were observed instead (Fig. 10).

Precise lattice parameter measurements of both α-Al and these modified $Al_3Sc$ particles reveal a shared value of 4.05 ± 0.005 Å, further supporting their crystallographic compatibility. Although the $Al_3Sc$ phase has been well reported, the other elements except Zr incorporation and its effects on the crystallography has rarely been reported.

According to the ICSD database, the $Al_3Sc$ is documented with crystallizes in a cubic structure with space group Pm-3m (221) and with a lattice parameter of $a$ = 4.105 Å [36]. The observed Al-Sc particles containing Ti in this study exhibit the same crystal structure as $Al_3Sc$, but with smaller lattice parameters (~4.05 Å) that are same as α-Al. This reduction in lattice parameter is attributed to compositional variations in the $Al_3Sc$ phase, including substitutional incorporation of Ti and other alloying elements i.e. Cu, Si, Mn, Zn), as well as trapped elements of Fe and Mn, and potential vacancy formation. Given the clearly resolved atomic substitution of Ti for Sc, these $Al_3Sc$ particles are more accurately described as $Al_3$(Sc,Ti) to reflect Ti incorporation.

The lattice parameters and formation energy variation of $Al_3$(Sc,Ti) with element incorporation was investigated with DFT calculation and shown in Figure 5. The $L1_2$-$Al_3X$ structure has a cubic lattice with space group Pm-3m (221). The X atoms are positioned at the Wyckoff 1a sites and Al at 3c. Alloying X in this phase lowers the symmetry of the system down.

Meanwhile, the calculations also showed that the frame of the structure remains with angles of the unit cells deviating less than 1 degree from 90°.

Figure 5a represents the dependences of lattice parameters on the Sc content in $L1_2$-$Al_3(Al_{1-x}Sc_x)$ (Figure 5a-a) and $L1_2$-$Al_3(Sc_{1-x}Ti_x)$ (Figure 5a-b), respectively. Obviously, the Ti incorporation into the $L1_2$-$Al_3(Sc_{1-x}Ti_x)$ structure caused the reduced lattice parameters. The lattice parameter decreases almost linearly with Ti content for the $L1_2$-$Al_3(Sc_{1-x}Ti_x)$ system (Figure 5a-b).

To account for the slight deviation of the Al/(Sc+Ti) ratio from the ideal 3:1, the effect of Al/Sc ratio variations on the lattice parameters is investigated here.It shows that the relation between the lattice parameter and the Sc content in $L1_2$-$Al_3(Al_{1-x}Sc_x)$ is more complex (Figure 5a-a). The lattice parameter increases quickly with addition of Sc. Then it increases slower with increases Sc content. The maximum difference between the calculated lattice parameter and the average value is at $x$(Sc) = 0.5. Then it creases moderately with Sc content.

Whether the incorporation of Ti into $Al_3Sc$ causes changes in the crystal structure is also investigated here. $Al_3Sc$ has a cubic $L1_2$-type structure, while the stable $Al_3Ti$ has the $D0_{23}$-type structure [37]. The investigation on the stability of $Al_3$(Sc,Ti) alloying compounds within three types of crystal structures, $L1_2$, $D0_{22}$ and $D0_{23}$ was presented in Figure 5b. It shows the Gibbs free energy of three different structures of $Al_3Sc$ with different Ti incorporation. $L1_2$-$Al_3$(Sc, Ti) and Ti in $L1_2$-$Al_3$(Al,Sc) crystals are displayed in Figure 5b. It shows that the $L1_2$-$Al_3$(Sc,Ti) has lowest formation energy until the Ti incorporation reach x(Ti) = 0.60 (60 wt.%), then the other types of structure ($DO_{22}$ and $DO_{23}$) become more stable. The $D0_{23}$-$Al_3$(Sc,Ti) becomes more stable in the Ti-rich part. This also demonstrates that, within the cooperative composition range of Ti (~0.5 wt.%), the $L1_2$-$Al_3$(Sc,Ti) phase remains the most stable crystal structure.

*3.3 Precipitation of Fe compounds within primary $Al_3$(Sc,Ti)*

The recycled Al alloy studied here is a multi-component system containing nine different alloying elements. $Al_3$(Sc,Ti), whether present as primary particles or as part of the eutectic phase, plays a critical role in the grain refinement of α-Al. As a single phase, the heterogeneous nucleation of α-Al primarily depends on structural templating [38], making the lattice mismatch at the nucleation interface a key factor. Therefore, understanding the effect of impurities on the lattice parameters of $Al_3$(Sc,Ti) is essential for elucidating its nucleation behaviour and guiding future alloy design and applications.

Further examination of the $Al_3$(Sc,Ti) particles revealed that, in some cases, brighter sub-particles are present within the primary $Al_3$(Sc,Ti) structure (Figure 6). SEM–EDS mapping shows that these bright regions are enriched in Fe, Mn, Cr and Si, indicating their unfavourable incorporation into the $Al_3$(Sc,Ti) lattice. Further investigation using STEM–EDS mapping (Figure 7) clearly reveals the presence of nanoscale Al–Fe–Mn–Si precipitates within the $Al_3$(Sc,Ti) particles highlighted by red dotted circles. Ti is uniformly distributed throughout the $Al_3$(Sc,Ti) nanofibers. In contrast, other elements such as Mg, Cu, Zn, and Si are primarily segregated at the surfaces of these $Al_3$(Sc,Ti) fibres.

*3.4 Evolution of Scandium distribution during alloy solidification*

The Al-Sc binary and RA-Sc multicomponent phase diagrams calculated using Pandat with the non-equilibrium Scheil model are shown in Figures 8a-b. As expected, the Al-Sc binary system exhibits a eutectic at 0.57 wt.% Sc (Figure 8a). The Scheil solidification path (Figure 8c) for an Al-1Sc alloy predicts that $L1_2$-$Al_3Sc$ solidifies firstly, followed by the binary eutectic reaction ($Al_3Sc$ + α-Al). It should be noted that although the Al–Sc binary system exhibits a eutectic composition at approximately 0.57 wt.% Sc, the solidification window for α-Al is extremely narrow (<1K), even when calculated using a non-equilibrium Scheil model. This limited temperature interval reduces the stability range of primary α-Al during the final stages of solidification. As a result, under metastable casting conditions, competitive formation may occur between primary α-Al and the binary eutectic reaction ($Al_3Sc$ + α-Al) in alloys with compositions close to the eutectic point.

In contrast, the situation changes dramatically in the multicomponent recycled alloy containing nine alloying elements. For the composition Al-1.33Si-1.28Mg-0.97Cu-0.88Zn-0.51Fe-0.57Mn-0.14Cr-0.09Ti, the equilibrium phase diagram predicts that primary $L1_2$-$Al_3Sc$ appears only above 1.94 wt.% Sc, far higher than the binary eutectic concentration. The Scheil solidification curve for the same alloy with 1 wt.% Sc (Figure 8d) shows that $Al_3Ti$ should solidify first, followed by $L1_2$-$Al_3Sc$ and subsequent reactions. However, the temperature interval in which equilibrium $Al_3Sc$ can form is extremely narrow (only ~0.1 K), meaning that under real casting conditions its formation is kinetically suppressed.

The non-equilibrium Scheil model was employed because it more realistically represents the rapid solidification behaviour and solute segregation occurring in multicomponent recycled Al alloys under casting conditions. Compared with equilibrium calculations, the Scheil model assumes complete mixing in the liquid phase and negligible diffusion in the solid phase, which better reflects the non-equilibrium nature of practical solidification processes. However, limitations still exist in current thermodynamic calculations for complex multicomponent recycled Al alloys, particularly due to uncertainties in thermodynamic databases, restricted diffusion assumptions, and the difficulty in accurately predicting phase evolution and micro-segregation behaviour in highly alloyed systems. The experimental observations expose limitations in current thermodynamic predictions for multicomponent Al alloys and demonstrate metastable Sc solidification behaviour in recycled compositions, underscoring an incomplete description of impurity effects on phase selection. Rather than equilibrium $Al_3Sc$ or $Al_3Ti$, a chemically modified primary phase, $Al_3(Sc,Ti)$, forms during solidification.

During the actual solidification sequence, partial of Sc was consumed for formation of primary $Al_3(Sc,Ti)$ particles and their surrounding eutectic shells. The remaining Sc is expected either to remain dissolved in the Al matrix or to precipitate later as secondary $Al_3(Sc,Ti)$ during subsequent cooling or heat treatment. Further experimental observations indicate that the Sc concentration exceeding the solubility limit in liquid Al during solidification is expected to form nanoscale $Al_3(Sc,Ti)$ rod-like precipitates, while the remaining Sc within the solid solubility limit is retained in the α-Al matrix. This residual Sc may subsequently precipitate during later heat-treatment processes, contributing to further strengthening of the alloy. Figure 9 shows STEM-HAADF image and corresponding STEM-EDS mappings, revealing long needle-like Sc-rich precipitates within the Al grains. The Ti concentration within these

$Al_3(Sc,Ti)$ rods is on average 2.01±0.02 wt.%, which is significantly lower than that measured in the primary $Al_3(Sc,Ti)$ particles. This is likely due to the rapid consumption of Ti during the formation of primary $Al_3(Sc,Ti)$ particles at higher temperature, resulting in a reduced Ti content in the subsequently formed $Al_3(Sc,Ti)$ rods, as shown in Table 3.

*3.5 Fe cluster and Impurity tolerance within $Al_3(Sc,Ti)$ precipitates*

The Sc-rich precipitates were further examined, as shown in Figure 10. Figure 10a presents a STEM-HAADF image of the precipitates from Figure 9a, revealing numerous bright clusters with irregular shapes. These precipitates were identified as $Al_3(Sc,Ti)$ with small crystal sizes and lattice parameters comparable to the primary $Al_3(Sc,Ti)$, and they exhibit excellent coherence with the surrounding Al matrix (Figures 10b-d). Occasionally, a few precipitates with Cu/Mg-rich can be observed at the surface of the $Al_3(Sc,Ti)$ particles, Fig. 10d. STEM–EDS mapping (Figure 10e) shows the distribution of all impurity elements in the alloy within and along the $Al_3(Sc,Ti)$ precipitates. Elements such as Si, Mg, Cu, Zn, and Mn are clearly segregated at the particle surfaces, whereas Fe, which is reported to be energetically unfavourable within $Al_3Sc$ [38], is present within the $Al_3(Sc,Ti)$ precipitates in clustered morphologies.

The further atomic-resolution STEM-EDS analysis (Fig. 11) provides additional evidence for the existence of Fe-enriched clusters within the $Al_3(Sc,Ti)$ particles. Figure 11 clearly shows that, although Fe is associated with the $Al_3(Sc,Ti)$ phase, it does not occupy specific ordered atomic positions within the lattice. In contrast, Ti exhibits a clear preferential occupation of the Sc sublattice sites. These results suggest that Fe exists as localised enriched clusters or segregated regions rather than as a substitutional element with well-defined crystallographic site occupancy.

The heat treatment experiment was designed based on conventional ageing temperatures, as a simple and quick approach to investigate the evolution of Fe clusters after ageing. The main aim was to examine whether Fe tends to form Fe-containing intermetallic compounds within $Al_3(Sc,Ti)$, or whether it is rejected from the particles and redistributed to other regions such as particle surfaces or interfaces. A heat treatment at 180 °C for 10 hours, the impurity distribution within and around the $Al_3(Sc,Ti)$ precipitates was examined (Figure 12). Ti, which was previously observed to be uniformly distributed within the $Al_3(Sc,Ti)$ precipitates (Figure 10e), becomes slightly segregated toward the centre after heat treatment (Figure 12d). Other impurity elements, including Si, Mn, Zn, Mg, and Cu (Figures 12f-j), show pronounced segregation at the precipitate surfaces. In addition, several Mg- and Si-rich precipitates were found to nucleate directly on the surfaces of the $Al_3(Sc,Ti)$ particles.

Notably, the distinct Fe-enriched clusters previously present inside of the $Al_3(Sc,Ti)$ precipitates before heat treatment become significantly redistributed after ageing at 180 °C for 10 h. As shown in Fig. 12, Fe is still detectable after heat treatment but mainly concentrated near the particle surface/interface regions instead of forming clearly defined internal clusters. This indicates diffusion and redistribution of Fe during the heat-treatment process. Figure 12k provides the Fe, Mn and Si concentration profiles along the line indicated in Figure 12a.Atomic-resolution STEM-EDS mapping of the interface between the $Al_3(Sc,Ti)$

precipitates and the Al matrix after heat treatment is shown in Figure 13. Clear segregation of Si, Mg, Mn, and Zn is detected at the precipitate surface, accompanied by slight atomic-scale lattice distortion (Figure 13a). Fe and Cu segregation is less apparent, likely due to their uneven distribution and lower local concentrations.

## 4. Discussion

### *4.1 Formation of primary $Al_3(Sc,Ti)$ and eutectic shell of ($Al_3(Sc,Ti)$ + α-Al)*

The phase diagram calculation for the multiple component recycled Al alloy Al-1.33Si-1.28Mg-0.97Cu-0.88Zn-0.51Fe-0.57Mn-0.14Cr-0.09Ti-1.0Sc predicated the formation of $Al_3Ti$ primary phase. Despite this prediction, the experimental results clearly show that the actual primary phase is $Al_3(Sc,Ti)$ rather than pure $Al_3Sc$ or $Al_3Ti$. This discrepancy can be explained as follows:

Firstly, because of the strong mutual solubility between Sc and Ti in the $L1_2$ structure, these elements readily co-substitute within the $Al_3X$ lattice, forming a stable $Al_3(Sc,Ti)$ solid solution across a wide compositional range. This co-substitution can reduce the nucleation barrier compared with forming pure $Al_3Sc$ or $Al_3Ti$, making $Al_3(Sc,Ti)$ the kinetically preferred phase during solidification.

Furthermore, although the phase-diagram calculations were performed using the Scheil model, which already represents non-equilibrium solidification, the actual cooling rate in this study (~3.5 K/s) is much faster and therefore far more non-equilibrium than the model assumptions. Under such conditions, solute segregation, diffusion constraints, and complex multi-element interactions further suppress the formation of pure equilibrium phases such as $Al_3Sc$ or $Al_3Ti$.

In addition, the large concentration difference between Sc (1.0 wt.%) and Ti (0.09 wt.%) favours the formation of an Sc-rich $Al_3X$ phase with Ti incorporation, rather than a Ti-rich variant. This preference is also supported by our DFT calculations (Figure 5), which show that Ti substitution into the $Al_3Sc$ lattice is energetically favourable.

Secondly, solute interactions within the multicomponent recycled Al alloy melt also play a significant role. The STEM analyses in this study clearly demonstrate interactions between $Al_3(Sc,Ti)$ particles and seven additional alloying or impurity elements: Fe, Cr, Si, Mn, Mg, Cu, and Zn. Many of these elements, including tramp elements such as Fe, Mn, and Cr, can be trapped into the $Al_3(Sc,Ti)$ particles at high solidification temperatures, and are later either rejected to the particle surface or precipitate internally as the temperature decreases.

Elements such as Si, Mg, Cu, Zn, Fe, and Mn influence the melt thermodynamics and diffusion behaviour during solidification. Their interactions with Sc and Ti might modify the effective liquidus temperatures and promote the stabilisation of mixed $Al_3(Sc,Ti)$ nuclei over the formation of the corresponding binary phases.

Another important phenomenon is the observation of a eutectic shell surrounding the primary $Al_3(Sc,Ti)$ particles. In most cases observed in this study, the primary $Al_3(Sc,Ti)$ becomes entirely covered by the eutectic ($Al_3(Sc,Ti)$ + α-Al). This eutectic contains nanoscale dendritic $Al_3(Sc,Ti)$, which grows outward from the underlying primary cube (Figures 2 and 4). As this layer develops, it progressively rounds off the sharp edges of the primary particle, producing a

ring-like or ball-like appearance. Consequently, the true morphology of the primary phase is easily obscured, which explains why eutectic $Al_3(Sc,Ti)$ could be misidentified as the primary phase.

As shown in Figure 8a, although the eutectic composition in the Al-Sc binary system is 0.57 wt.% Sc, the solidification window for α-Al is extremely narrow (less than 1 K). Therefore, at the final stage of primary $Al_3(Sc,Ti)$ solidification, a metastable eutectic reaction of $Al_3(Sc,Ti)$ + α-Al may nucleate and solidify prior to the independent nucleation of α-Al. Consequently, a eutectic shell forms around the primary $Al_3(Sc,Ti)$ particles, in which $Al_3(Sc,Ti)$ nucleates heterogeneously on the primary particles and acts as the leading phase.

*4.2 Impurity tolerance and its effect on $Al_3(Sc,Ti)$ crystal structure and formation*

Atomic-resolution STEM–EDS mapping (Figure 4) confirms that Ti preferentially substitutes for Sc within the $L1_2$ lattice. Density functional theory (DFT) calculations show that Ti incorporation slightly reduces the lattice parameter without disrupting the $L1_2$ structure, consistent with experimental observations.

Other alloying elements, including Fe, Mn, Si, Cu, Mg, and Zn, do not occupy well-defined crystallographic sites. Instead, they are incorporated randomly, segregate to lattice defects, or reside at particle interfaces. This lack of positional preference likely arises from low local concentration, lattice strain accommodation, and metastable trapping during rapid precipitation.

The formation of $Al_3(Sc,Ti)$ in multicomponent recycled aluminium alloys is strongly influenced by high impurity content. STEM analyses show that $Al_3(Sc,Ti)$ accommodates a wide range of solutes, including Fe, Cr, Si, Mn, Mg, Cu, and Zn, even though many, such as Fe, are theoretically energetically unfavourable within the $Al_3Sc$ lattice. This reflects the intrinsic impurity tolerance of the $L1_2$-$Al_3X$ structure, which features a relatively open Al sublattice and flexible bonding environment, allowing transient accommodation of foreign atoms without disrupting overall crystal symmetry.

During early-stage solidification at high temperatures, tramp elements such as Fe, Mn, and Cr can be temporarily incorporated into both primary and eutectic $Al_3(Sc,Ti)$. These solutes are unstable within the lattice and subsequently precipitate, as shown in Figure 6. Due to their differing atomic radii and bonding characteristics relative to Sc and Ti, they introduce local lattice distortions and increase elastic strain energy, contributing to particle refinement and the formation of defects such as twinning and face-cantered voids (Figure 3).

Although only Fe-rich clusters were clearly observed experimentally, Mn and Cr were also detected within the $Al_3(Sc,Ti)$ particles. The differences in their clustering behaviour are likely related to several factors. Firstly, the atomic interactions within the $Al_3(Sc,Ti)$ phase should be considered. Experimental results demonstrate that the major atomic species occupying specific lattice positions in $Al_3(Sc,Ti)$ are Al, Sc, and Ti. Therefore, impurity tolerance is expected to depend strongly on the atomic interactions between Al–X, Sc–X, and Ti–X (where X = Fe, Mn,

or Cr). According to literature data [39], the mixing enthalpy values $\Delta H_{AB}^{mix}$ (KJ/mol) are: Al–Fe (-11), Al–Mn (-19), Al–Cr (-10); Sc–Fe (-11), Sc–Mn (-8), Sc–Cr (1); Ti–Fe (-37), Ti–Mn (-8), and Ti–Cr (-7). These values indicate that the interactions between impurity elements and the matrix-forming elements can differ significantly. In particular, the interactions involving Sc vary considerably among Fe, Mn, and Cr. Since the studied alloy contains nine different alloying elements, the overall elemental interactions become highly complex, which also highlights the current challenges in fully understanding the underlying physics of recycled Al alloys. In this work, we report this novel phenomenon with strong experimental evidence and provide discussion to assist in understanding the observed results. Secondly, the different clustering behaviours may also be related to the differences in solubility and concentration among Fe, Mn, and Cr. In the present alloy, the Cr concentration is relatively low (0.14 wt.%), which may explain why no obvious Cr-rich clusters were observed. Although the concentrations of Fe (0.51 wt.%) and Mn (0.57 wt.%) are comparable, Mn has a significantly higher solid solubility in Al than Fe at the formation temperature of $Al_3$(Sc,Ti). As a result, Fe is more likely to segregate and form clusters, whereas Mn tends to remain more uniformly distributed within the matrix.

As the temperature decreases, the $Al_3$(Sc,Ti) lattice progressively rejects these distortions, resulting in surface segregation or nanoscale precipitate formation. In fine $Al_3$(Sc,Ti) precipitates (Figure 9), formed at lower temperatures, the driving force for Fe-rich intermetallic formation or segregation is weaker, allowing some Fe-rich clusters to remain. Heat treatment (Figure 10) further promotes surface segregation, confirming continued redistribution.

Impurities also influence $Al_3$(Sc,Ti) formation and crystallography. Elements such as Si, Mg, Cu, Zn, Fe, and Mn modify melt activity and diffusion, shifting effective liquidus temperatures, reducing the driving force for binary $Al_3Sc$ formation, and promoting mixed $Al_3$(Sc,Ti) nucleation with higher solute tolerance. The combined effects of lattice mismatch, elastic strain, and defect formation during high-temperature incorporation explain the defect generation face-cantered voids in this study, and subsequent trapped-then-rejected behaviours of these impurities.

### *4.3 Quantification and Implications of Impurity Tolerance*

$Al_3$(Sc,Ti) particles exhibit a strong capability to trap impurities regardless of whether they solidify as primary phases at high temperature or precipitate at lower temperatures. Although incorporation of these impurities is thermodynamically unfavourable at low temperature, leading to subsequent precipitation or rejection, the initial trapping is clearly observed and quantified.

Since the majority of Fe, Mn, and Si precipitate within $Al_3$(Sc,Ti) during solidification, their exact tolerance limits are difficult to determine. For simplicity, a conservative assumption is made that all $Al_3$(Sc,Ti) particles possess the same tolerance. Based on this, calculated limits according to the average composition of $Al_3$(Sc,Ti) precipitates listed in Table 3, are:

0.115 wt.% Si, 0.096 wt.% Ti, 0.016 wt.% Mn, 0.030 wt.% Fe, 0.061 wt.% Cu, 0.056 wt.% Zn, 0.017 wt.% Cr, and 0.025 wt.% Mg, corresponding to a total of ~0.26 wt.%.

This impurity-trapping capability reduces element concentrations in the α-Al matrix, suppresses coarse Fe-rich intermetallic, improves microstructural stability, mitigates segregation, and enhances crack resistance and corrosion performance. In recycled aluminium alloys, where impurity levels are higher, $Al_3(Sc,Ti)$ formation provides a critical benefit by increasing impurity tolerance while maintaining mechanical performance.

*4.4 Mechanism of Impurity Tolerance in $Al_3(Sc,Ti)$*

Beyond strengthening, Sc plays a critical role as a performance-enhancing element for Al alloys. This first-time reported impurity tolerance capability is therefore highly significant, not only for casting alloys, where impurity control is crucial, but also for the design of sustainable and resilient Al alloys. By accommodating a wide range of impurity elements, $Al_3(Sc,Ti)$ enables optimized heat-treatment precipitation and microstructural control, maximizing alloy performance while supporting the use of recycled or lower-purity feedstock.

$Al_3(Sc,Ti)$ accommodates a wide range of elements (Cu, Si, Ti, Zn, Fe, Mn, Cr) across the periodic table, with widely varying atomic radii, electronic structures, and bonding preferences (metallic, covalent, or mixed). Among these, only Ti clearly substitutes for Sc in the $L1_2$ lattice; other elements are incorporated randomly, segregate to defects or interstitial sites, or are below experimental detection limits.

This chemical flexibility surpasses that of Fe-rich intermetallic compounds, which tolerate substitution only for certain 3d metals at Fe sites and Si at Al sites [40-42]. The underlying mechanism reflects non-equilibrium, defect-mediated incorporation during solidification and early-stage precipitation. The primary $Al_3(Sc,Ti)$ forms at temperature higher than 600 °C with high atomic diffusivity, elevated vacancy concentrations, and local solute segregation. Under these conditions, impurity atoms are kinetically trapped at the solid/liquid interface before partitioning into stable intermetallic phases, allowing metastable deviations from the ideal 3:1 stoichiometry.

At the atomic scale, Sc's partially filled 3d orbitals facilitate strong d–d bonding with Fe, Mn, and Ti, metallic bonding with Cu and Zn, and notable affinity for Si. These interactions partially offset the substitutional energy penalty. Structurally, the $L1_2$ lattice is simple, with a measurable homogeneity range, tolerates antisite defects and vacancy-assisted substitution, particularly at high formation temperatures [43, 44]. Elastic strain from impurity substitution can relax at high temperature, with excess solute rejected upon cooling forming Al-Fe-Mn-Si precipitates and stabilizing the crystal. Central cavities observed in Figure 3 indicate internal stress relaxation associated with solute redistribution.

In contrast, Fe-rich intermetallic compounds have complex ordered structures, narrow homogeneity ranges, and strongly directional bonding, limiting compositional flexibility. Therefore, the exceptional impurity tolerance of $Al_3(Sc,Ti)$ arises from high-temperature non-

equilibrium solidification, defect-mediated solute incorporation, local Sc–X bonding, and $L1_2$ lattice flexibility.

## 5 Conclusions

(1) The $Al_3Sc$ phase formed in the recycled alloy Al-1.33Si-1.28Mg-0.97Cu-0.88Zn-0.51Fe-0.57Mn-0.14Cr-0.09Ti-1Sc was modified through Ti and the other impurities incorporation, yielding an $Al_3(Sc,Ti)$ phase with a reduced lattice parameter of $a$ = 4.05 ± 0.005 Å. The lattice misfit between $Al_3(Sc,Ti)$ and α-Al was essentially zero, indicating excellent crystallographic compatibility.

(2) Primary $Al_3(Sc,Ti)$ particles were consistently enveloped by a eutectic ($Al_3(Sc,Ti)$ + α-Al) structure. The primary particles displayed cubic morphologies, occasionally containing central voids that evolved from faceted to rounded shapes. The eutectic $Al_3(Sc,Ti)$ exhibited fibrous or dendritic morphologies, forming ring-like shells that gradually transitioned from cubic to near-spherical forms.

(3) Both primary and eutectic $Al_3(Sc,Ti)$ shared identical chemistry and crystallography ($L1_2$, $a$ = 4.05 ± 0.005 Å), indicating formation of the same phase across different solidification regimes.

(4) Atomic-resolution STEM–EDS analysis confirms that Ti is incorporated into the $Al_3(Sc,Ti)$ structure by substituting for Sc atomic sites. Density functional theory (DFT) calculations further demonstrate that Ti substitution reduces the lattice parameter of $Al_3Sc$ while preserving the $L1_2$ crystal structure within the investigated compositional range (Ti content below 60% of the Sc sublattice).

(5) Although Fe is thermodynamically unfavourable in $Al_3Sc$, it can be transiently incorporated during solidification at a cooling rate of 3.5 K/s. Fe subsequently precipitated within the $Al_3(Sc,Ti)$ or segregated as nanoscale clusters during the final stages of solidification.

(6) The Fe-rich clusters within $Al_3(Sc,Ti)$ can be rejected to the interface of $Al_3(Sc,Ti)$/Al after long time heat treatment, i.e. 180 $^oC$*10 hrs.

(7) Atomic-resolution STEM–EDS analysis reveals no apparent preferential site occupancy for the trapped elements (Si, Mn, Fe, Cu, Mg, and Zn) within the $Al_3(Sc,Ti)$ lattice, suggesting a largely random or defect-assisted incorporation mechanism rather than ordered substitution on specific crystallographic sites.

(8) The tolerance of Si and Mn within $Al_3(Sc,Ti)$ is partially relieved through the precipitation of Fe-rich intermetallic compounds or through elemental segregation during subsequent solidification and cooling. In contrast, Cu, Mg, and Zn are predominantly rejected from the particle interior and segregate to the surface of $Al_3(Sc,Ti)$, indicating limited bulk solubility and a preference for interfacial accommodation.

(9) Although Ti exhibits an energetically favourable substitution for Sc within the $Al_3(Sc,Ti)$ lattice, post-heat-treatment observations indicate that Ti tends to segregate and form Ti-rich domains within the $Al_3(Sc,Ti)$ particles rather than being rejected to the particle surface. This behaviour suggests local compositional redistribution driven

by thermodynamic stabilization at lower temperatures while maintaining the overall $L1_2$ framework.

**Author Contributions**:

Conceptualization, methodology, Experimental investigation, writing, review & editing, funding acquisition: Z. Q.;

STEM: R. N.;

DFT calculation: C.M. Fang.

All authors have read and agreed to the published version of the manuscript.

**Funding:** This work was financial supported by the EPSRC (UK) under grant number EP/N007638/1 (Future Liquid Metal Engineering Hub) and by Brunel University of London BRIEF award (11937131).

**Conflicts of Interest**: The authors declare no conflict of interest.



**References**

1. The Role of Critical Minerals in Clean Energy Transitions. International Energy Agency (2021).
2. Aluminium Recycling. International Aluminium Institute (2023).
3. Aluminium in the Circular Economy. European Aluminium (2022).
4. Greenhouse Gas Pathways to 2050. International Aluminium Institute (2023).
5. Aluminium, Tracking Clean Energy Progress. International Energy Agency (2022).
6. D. Rabbe, D. Ponge, P. J. Uggowitzer, M. Roscher, et. al. Making sustainable aluminum by recycling scrap: The science of "dirty" alloys, Prog. Mater. Sci., 128 (2022) 100947.
7. R. G. Billy, D. B. Müller. Aluminium use in passenger cars poses systemic challenges for recycling and GHG emissions. Resour. Conserv. Recycl., 190 (2023) 106827.
8. G. Gaustad, E. Olivetti, R. Kirchain. Improving aluminum recycling: A survey of sorting and impurity removal technologies. Resour. Conserv. Recycl., 58 (2012) 79-87.
9. Z. Niu, Z. Que, J.B. Patel, Z. Fan. Assessment and Improvement of Melt Quality of Recycled Secondary A357 Alloy by Application of the High Shear Melt Conditioning (HSMC) Technology. Crystals, 14(12) (2024) 1044.
10. B.S. Murty, S.A. Kori, M. Chakraborty. Grain refinement of aluminium and its alloys by heterogeneous nucleation and alloying. Int. Mater. Rev., 47(1) (2002) pp.3-29.
11. Q. Zheng, J. Wu, R. Cao, T. Chen, W. Wei, S. Yang. Recent advances in grain refinement of aluminum alloys: Nucleant particles and solute effects. J. Mater. Res. Techno., 39 (2025) pp.5720-5750.
12. J. Røyset, N. Ryum. Scandium in aluminium alloys. Int. Mater. Rev., 50(1) (2005) 19-44.
13. Q. Li, X. Liu, J. Wang, C. Xue, S. Wang. Boosting the grain refinement of commercial Al alloys by compound addition of Sc. J. Mater. Res. Techno., 28 (2024) pp. 1774-1783.

14. Z. Lei, S. Wen, H. Huang, W. Wei, Z. Nie. Grain Refinement of Aluminum and Aluminum Alloys by Sc and Zr. Metals, 13(4) (2023), 751.
15. S. Liu, X. Wang, Q. Zu, B. Han, X. Han, C. Cui. Significantly improved particle strengthening of Al–Sc alloy by high Sc composition design and rapid solidification. Mater. Sci. Eng. A, 800 (2021) 140304.
16. R. Ding, J. Deng, X. Liu, Y. Wu, Z. Geng, D. Li, T. Zhang, C. Chen, K. Zhou. Enhanced mechanical properties and thermal stability in additively manufactured Al-Ni alloy by Sc addition. J. Alloys Compd., 934 (2023), 167894.
17. C. Yang, P. Cheng, B. Chen, J. Zhang, G. Liu, J. Sun. Solute clusters-promoted strength-ductility synergy in Al-Sc alloy. J. Mater. Res. Techno., 96 (2022) 325-331.
18. J-Y. Zhang, Y-H Gao, P. Zhang, J. Kuang, G. Liu, J. Sun. Microalloying Al alloys with Sc: a review. Rare Metals, 39 (2020) 636-650.
19. Z. Lu, X. Wu, J. Xu, H. Zhang, L. Yu, L. Zhao, Y. Jiang. Improving mechanical properties of spray formed 7055 aluminium alloy metal-inert gas welds by scandium addition. J. Alloys Compd., 1013 (2025) 178406.
20. F. Ahmad , V. B. Rajendren, X. Kai, S.S.A. Shah, S. Ullah Khan, S.M. Dar, A. Naveed, A. W. Zia, Y. Zhao. Role of scandium addition to microstructure, corrosion resistance, and mechanical properties of AA7085/$ZrB_2$+$Al_2O_3$ composites. J. Alloys Compd., 1005 (2024) 176065.
21. G. Du, J. Deng, Y. Wang, D. Yan, L. Rong. Precipitation of (Al,Si)3Sc in an Al-Sc-Si alloy. Scr. Mater. 61 (2009) 532-535.
22. Y. Harada, D.C. Dunand. Microstructure of Al3Sc with ternary transition-metal additions. Mater. Sci. Eng. A 329-331 (2002) 686-695.
23. C.B. Fuller, D.N. Seidman. Temporal evolution of the nanostructure of Al(Sc,Zr) alloys: Part II-coarsening of $Al_3(Sc_{1-x}Zr_x)$ precipitates. Acta Mater. 53 (2005) 5415-5428.
24. M. Song, Y.H. He. Investigation of primary $Al_3$(Sc,Zr) particles in Al-Sc-Zr alloys. Mater. Sci. Technol. (27(1) (2011) 431-433.
25. Y. Harada, D.C. Dunand. Creep properties of Al3Sc and Al3(Sc,X) intermetallics. Acta Mater. 48 (2000) 3477-3487.
26. J. Dumbre, S.K. Kairy, E. Anber, T. Langan, M.L. Taheri, T. Dorin, T., N. Birbilis. Understanding the formation of $(Al, Si)_3Sc$ and V-phase ($AlSc_2Si_2$) in Al-Si-Sc alloys via ex situ heat treatments and in situ transmission electron microscopy studies. J. Alloys Compd. 861 (2021)158511.
27. Z. Que, Z. Niu, C.L. Mendis, R.F. Negrea, Z. Fan. Growth twinned ($Al_3$(Sc,Ti) +α-Al) eutectic cells enable novel grain refinement in recycled Al alloys. Materials and Design, accepted, May 2026.
28. Z. Que, et. al. ongoing research.
29. J. R. Davis. (Ed.). Aluminum and aluminum alloys. ASM International. (1993).
30. Aluminium Association: Standard Test Procedure for Aluminium Alloy Grain Refiners: TP-1, Washington DC., (1987).
31. E. Scheil. Bemerkungen zur Schichtkristallbildung. Z. Met. 34, (1942) 70-72.

32. G. Kresse, J. Furthmüller. Efficiency of ab-initio total energy calculations for metals and semiconductors using a plane-wave basis set, Comp. Mater. Sci., 6 (1996) pp.15–50.
33. J. P. Perdew, K. Burke, M. Ernzerhof. Generalized gradient approximation made simple. Phys. Rev. Lett. 77, (1996) pp.3865-68.
34. P. E. Blőchl. Projector augmented-wave method, Phys. Rev. B. 50 (1994) pp.17953–17978.
35. H. J. Monkhorst, J. D. Pack. Special points for Brillouin-zone integrations, Phys. Rev. B. 13 (1976) pp.5188–5192.
36. I.I. Zalutskii, P.I. Kripyakevich. R Al3 compounds in rare earth- aluminium systems and their crystal structures. Kristallografiya, 12 (3) (1967) pp. 394-397.
37. P. Norby, A.N. Christensen. Preparation and structure of Al3Ti. Acta Chem. Scand., Ser. AA: Physical and Inorgranic Chemistry 40 (1986) pp. 157-159. ICSD 58189.
38. Z. Fan. An Epitaxial Model for Heterogeneous Nucleation on Potent Substrates. Metall. Mater. Trans. A, 44 (2013) pp. 1409-1418.
39. A. Takeuchi, A. Inoue. Classification of bulk metallic glasses by atomic size difference, heat of mixing and period of constituent elements and its application to characterization of the main alloying element. *Mater. Trans.*, 46 (2005) 2817–29.
40. Z. Que, C. Fang, C.L. Mendis, Y. Wang, Z. Fan. Effects of Si solution in θ-$Al_{13}Fe_4$ on phase transformation between Fe-containing intermetallic compounds in Al alloys. J. Alloys Compd., 932 (2023) 167587.
41. Z. Que, C. Fang, J. Xia, Z. Fan. Influences of Zr and V Addition on the Crystal Chemistry of θ-$Al_{13}Fe_4$ and the Grain Refinement of α-Al in an Al-4Fe Alloy Based on Experiment and First-Principle Calculations. Crystals, 14(10) (2024) 879.
42. Y. Cai, R. Liang, L. Hou, J. Zhang. Effect of Cr and Mn on the microstructure of spray-formed Al-25Si-5Fe-3Cu alloy. Mater. Sci. Eng. A, 528 (2011) pp. 4248-4254.
43. S. Liu, B. Liao, B. Nie, T. Fan, D. Chen, J. Zhang, Y. Song. First-Principles Study of Atomic Diffusion by Vacancy Defect of the $L1_2$-$Al_3M$ (M = Sc, Zr, Er, Y) Phase. Molecules, *28*(18) (2023) 6727.
44. Y. Meng, S, Wang, H. Su, C. Zhang, B. Wang, C. Xue, J. Wang. The Effect of Point Defects on Young's Modulus of the Off-Stoichiometric $Al_3X$ (X = Li, Sc, and Zr) Phases: A First-Principles Study. Metals, 14(1) (2024) 30.

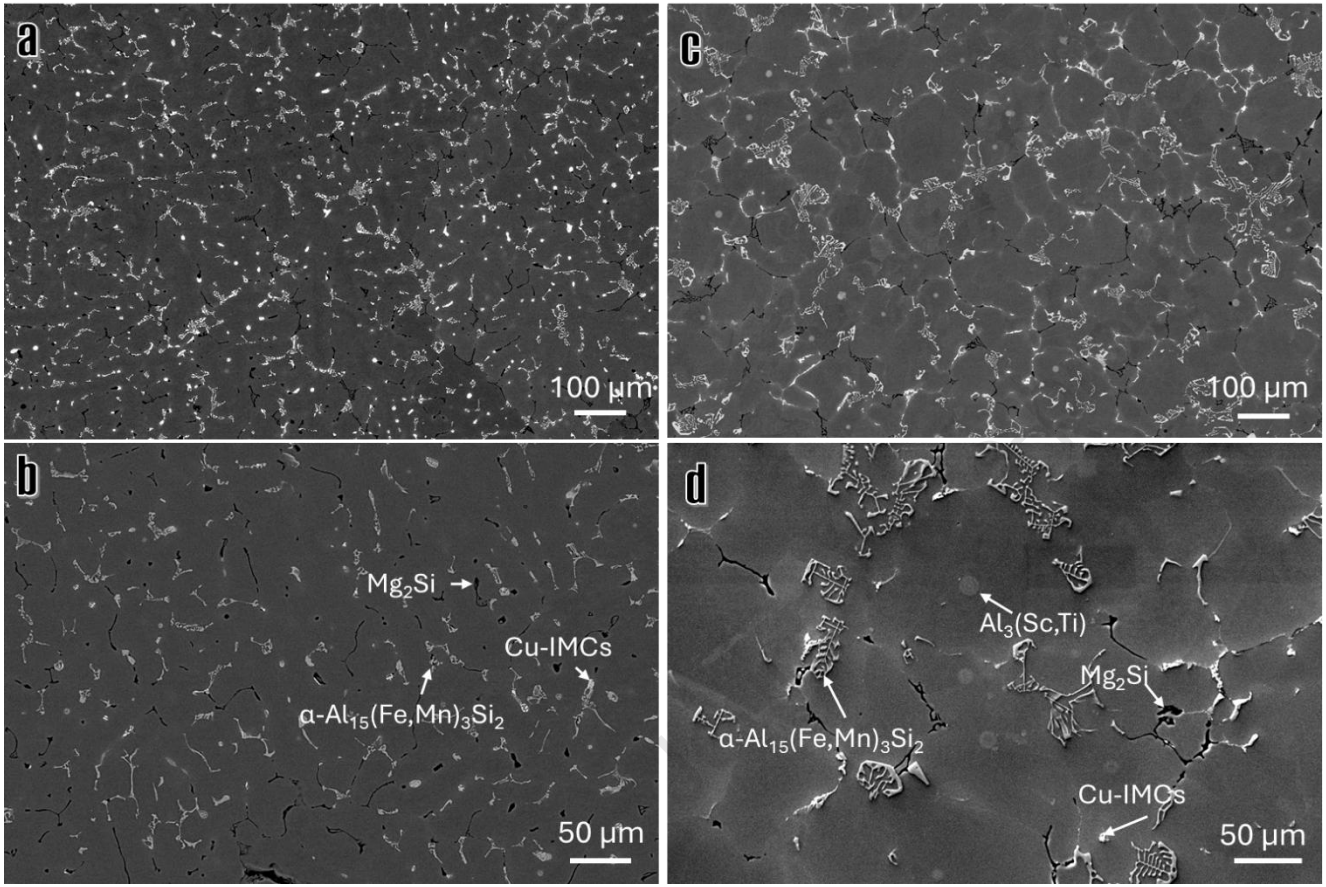


Figure 1 SEM-BSD images showing the as-cast microstructure of the studied recycled Al alloy solidified at 3.5K/s (a, b) without addition of Sc, consisting of primary α-Al, eutectic α-$Al_{15}(Fe,Mn)_3Si_2$, $Mg_2Si$ and Cu-IMCs; and (c, d) RA+1.0wt.% Sc, consisting of primary $Al_3(Sc,Ti)$ distributed within α-Al grains, eutectic α-$Al_{15}(Fe,Mn)_3Si_2$, $Mg_2Si$ and Cu-IMCs.

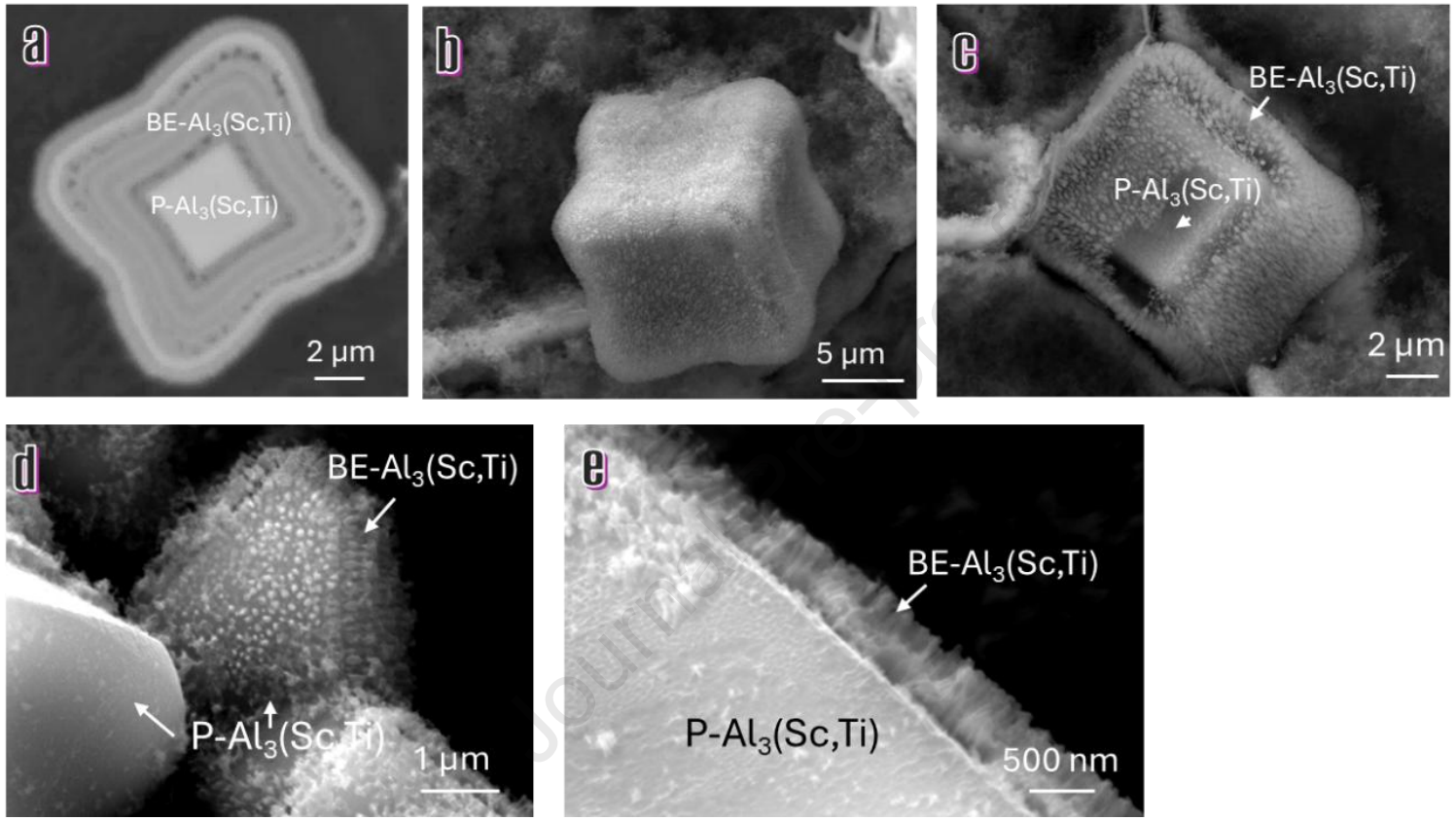


Figure 2 SEM images showing (a) cubic primary (solid) $Al_3(Sc,Ti)$ particles covered with layer-by-layer binary eutectic (BE) ($Al_3(Sc,Ti)$ + α-Al); (b) 3D morphology showing the BE-($Al_3(Sc,Ti)$ + α-Al) fully covered the primary $Al_3(Sc,Ti)$; (c) 3D morphology cover by the BE-shells and the BE structure is villiform; (d-e) high magnification SEM showing the villose BE structure grows on the central primary $Al_3(Sc,Ti)$.

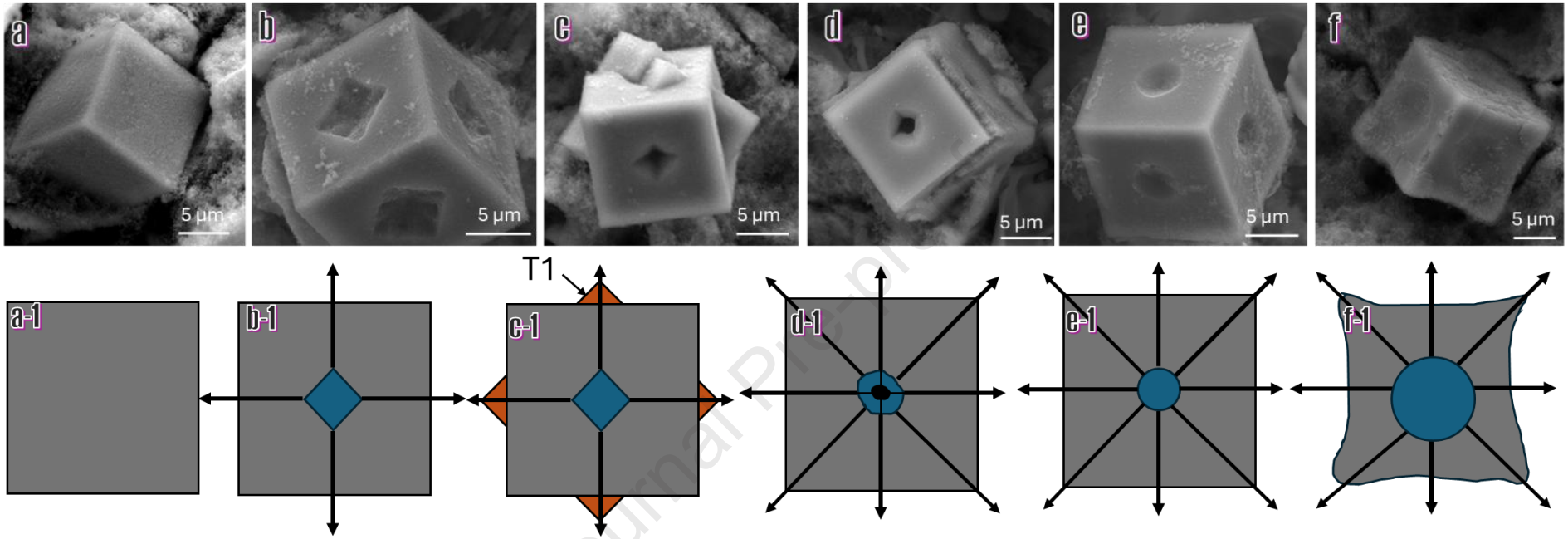


Figure 3 (a-f) SEM and corresponding ((a-1)-(f-1))schematic diagram images showing the 3-dimensional (3D) morphology and the morphology evolution of $Al_3(Sc,Ti)$ particles: (a) the ideal cubic; (b) the cubic with face central square hole; (c) the 45° rotated twins within the cubic; (d) the cubic with face-central curved square hole; (e) the cubic with face-central round hole; (f) the cubic with face-central round hole and bended faces.

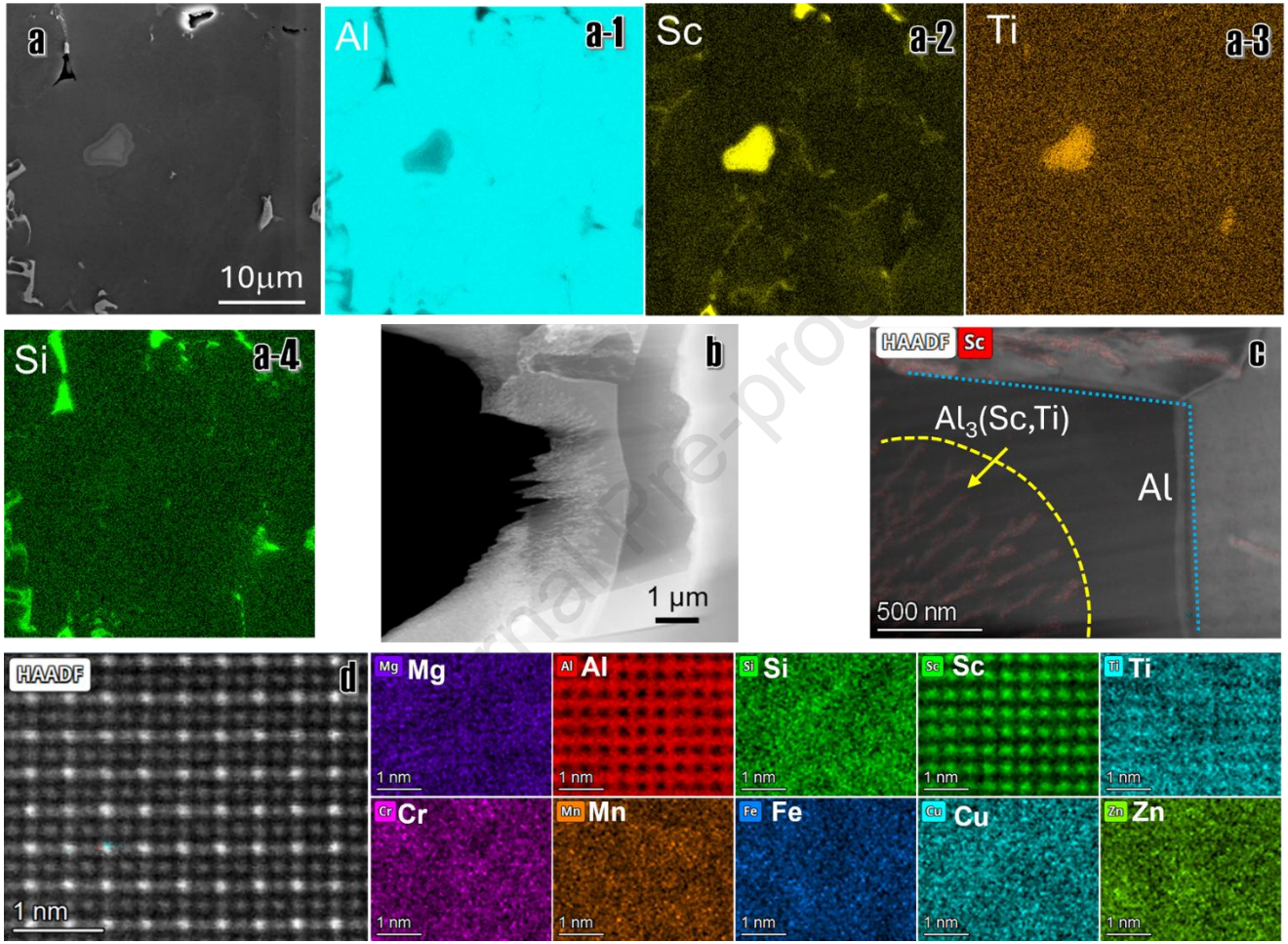


Figure 4. (a) SEM-EDS mapping demonstrates these particles are Sc and Ti rich, the eutectic area consisted the Al concentration variation; (b) STEM-HAADF image further confirmed the outer area (BE) are two phase ($Al_3(Sc,Ti)$ + α-Al) and the $Al_3(Sc,Ti)$ is in dendritic morphology; (c) although the BE-($Al_3(Sc,Ti)$ + α-Al) surface looks curved under SEM, it actually terminated with cubic faceted. (d) atomic resolution HAADF image and atomic resolution STEM-EDS mapping showing the elemental distribution inside the Al-Sc-Ti particle.

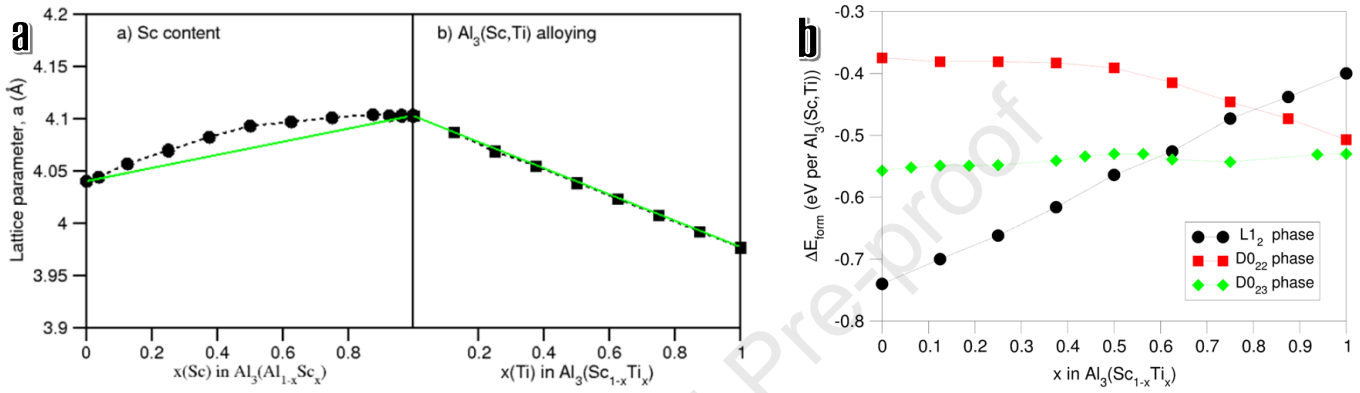


Figure 5. DFT calculation results showing (a) variation of lattice parameters normalized for the primary unit cell on the Sc content in $L1_2$-$Al_3(Al_{1-x}Sc_x)$ and $L1_2$-$Al_3(Sc_{1-x}Ti_x)$ alloying compounds. The green lines represent the averaged values between those of the α-Al and $L1_2$-$Al_3Sc$ in Figure 5a and the $L1_2$-$Al_3Sc_x$ and $L1_2$-$Al_3Ti$ in Figure 5b, respectively; (b) Formation energy of different types of crystal structure of $Al_3X$ particles with different Ti incorporation which demonstrate the lowest energy of $LI_2$-$Al_3X$ at Ti concentration lower than 0.5.

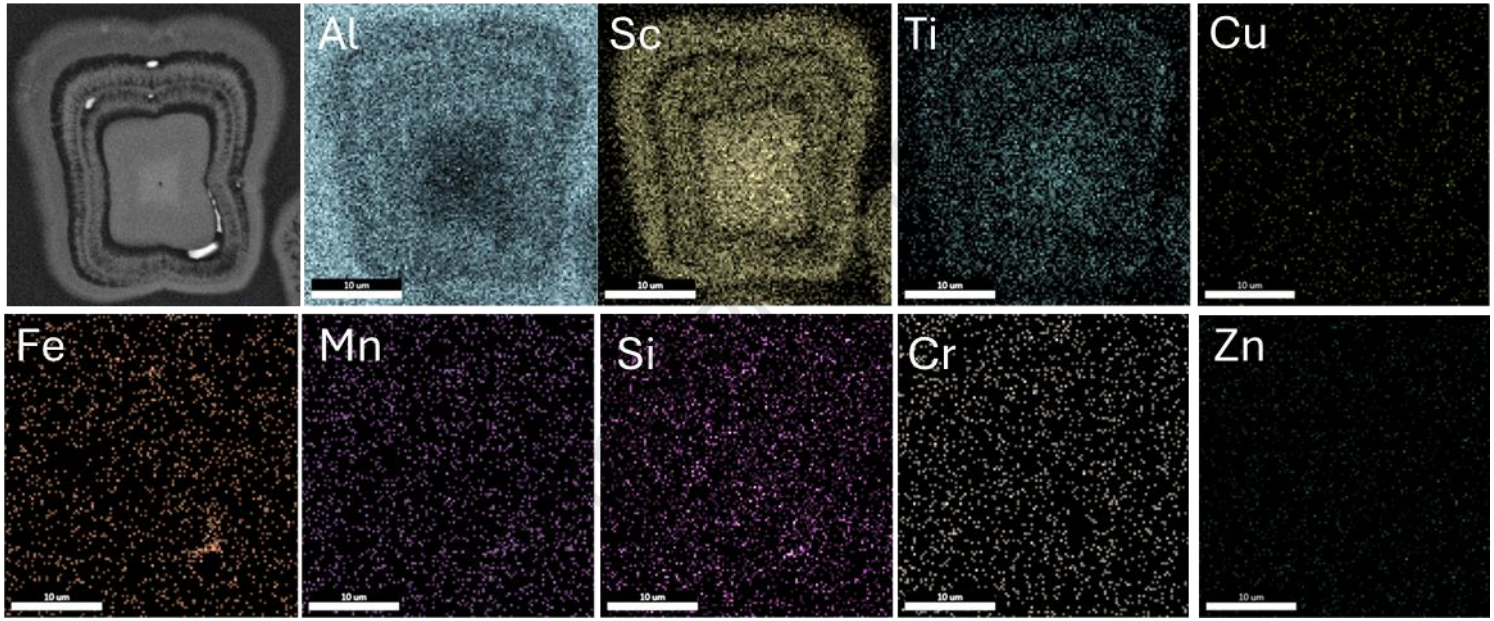


Figure 6. SEM-EDS mapping on a $Al_3(Sc,Ti)$ particle containing bright particles which demonstrating the bright particles are Al-Fe-Mn-Si rich particles,

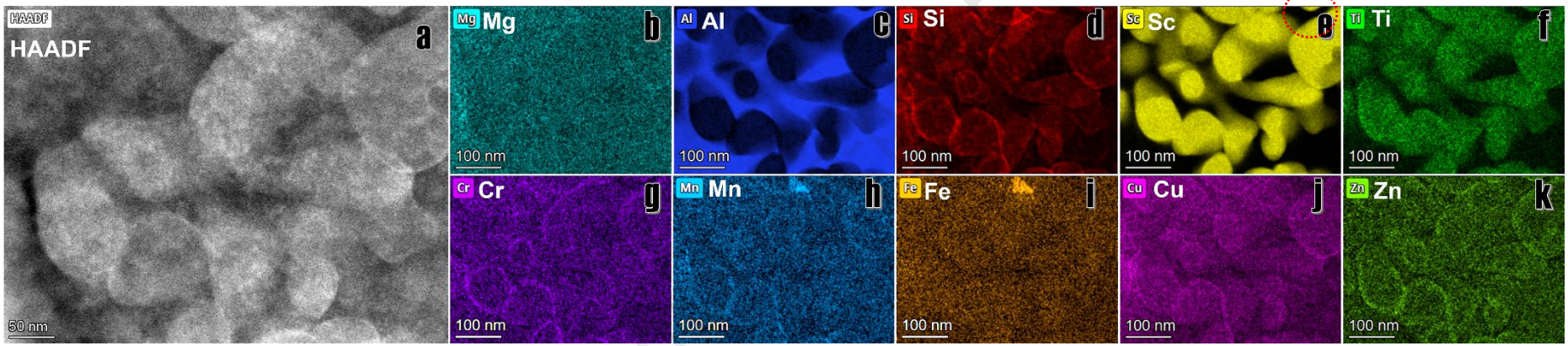


Figure 7. STEM-EDS mapping result indicating the elemental distribution within this Sc-rich particles composed mainly containing Al, Sc, Ti. Elemental segregation was observed along the Sc-rich dendritic regions, particularly for Si, Cu and Zn. In addition, a nanometre-scale precipitate enriched with Si, Fe and Mn were detected. (a) HAADF; (b) Mg; (c) Al; (d) Si; (e) Sc; (f) Ti; (g) Cr; (h) Mn; (i) Fe; (j) Cu; (k) Zn.

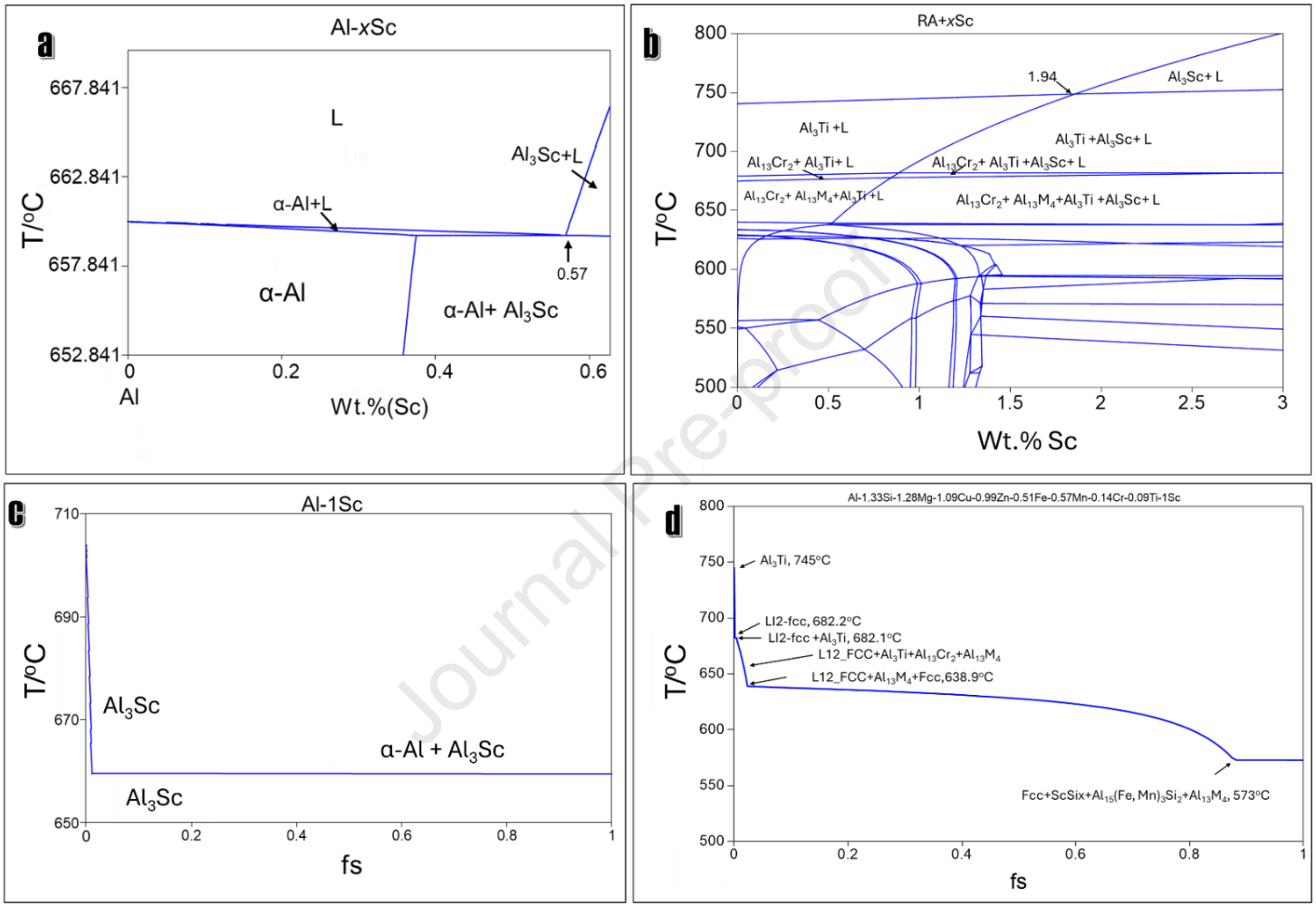


Figure 8. Calculated phase diagram with Pandat software under Scheil model (a) Al-*x*Sc binary alloys; (b) RA-*x*Sc multiple component alloys; (c) solidification curve of Al-*1*Sc binary alloy; (d) solidification curve of RA+ 1Sc alloy.

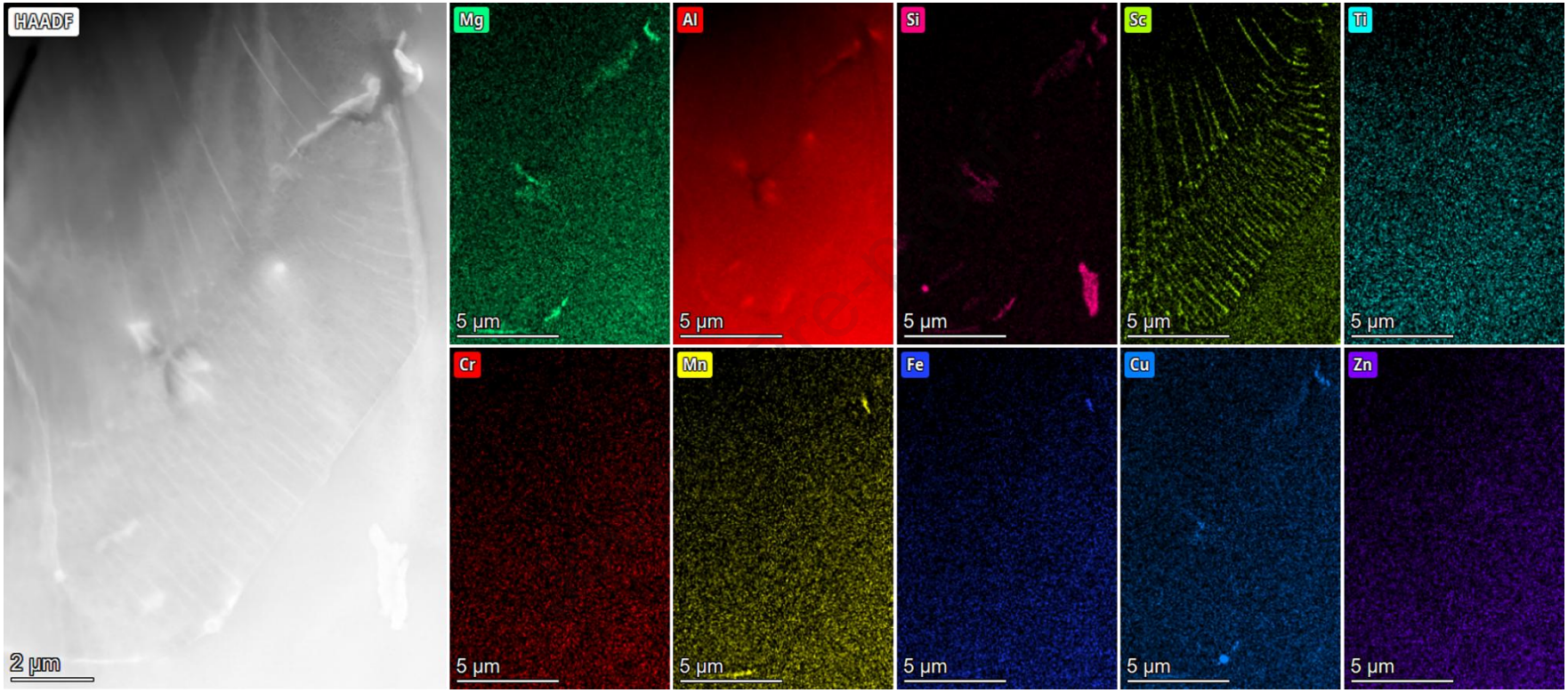


Figure 9. STEM-HAADF showing the $Al_3(Sc,Ti)$ precipitates on the Al matrix within the Al grains. The corresponding STEM-EDS mapping confirms that the long needle-like precipitates are Sc-IMCs, together with some Cu-rich and Fe/Mn-rich nanometre-scale precipitates.

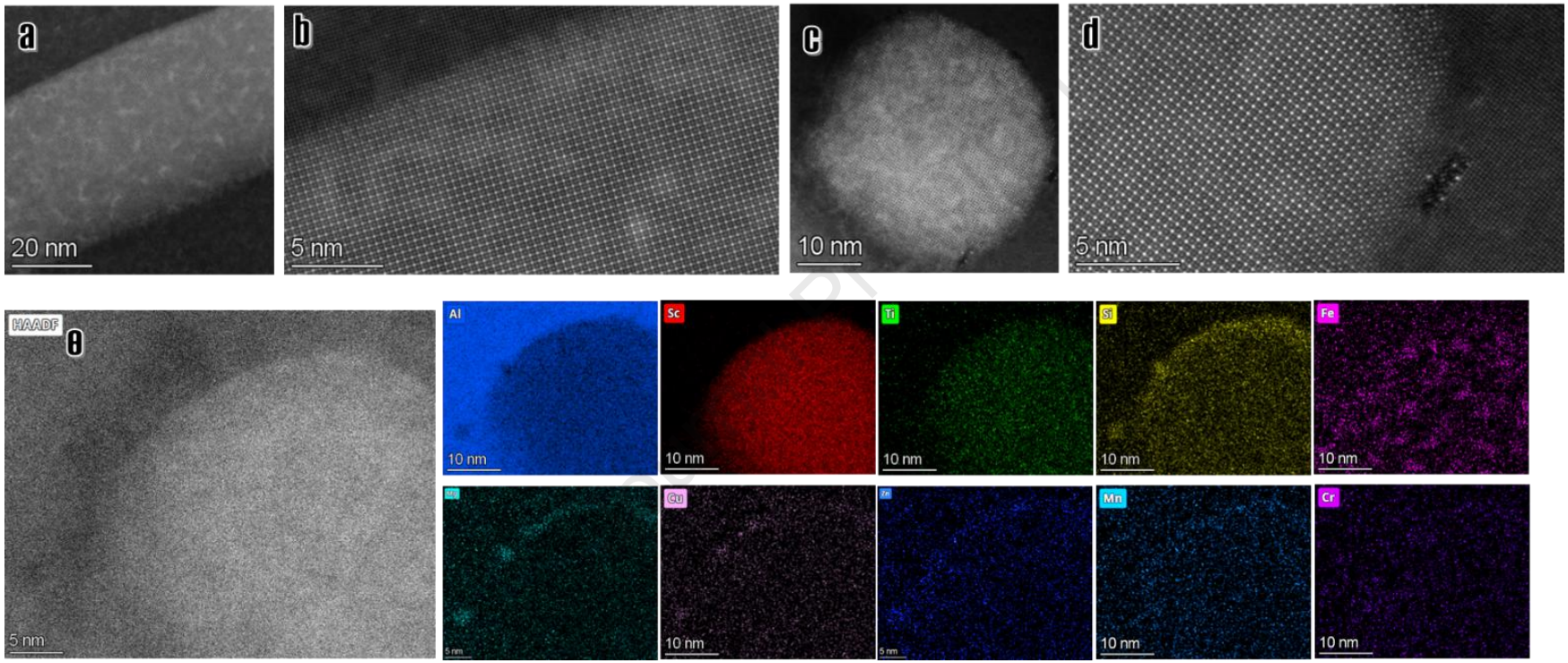


Figure 10. (a-e) HAADF images showing: (a) some brighter cluster-like patterns on $Al_3(Sc,Ti)$ needles along the longitude direction; (b) the high resolution HAADF confirms the brightness patterns; (c) the cluster-pattern on $Al_3(Sc,Ti)$ needles along the cross section; (d) some precipitates associated with the surface of the $Al_3(Sc,Ti)$ particles; (e) STEM-EDS mapping of particle (c) which demonstrates the Fe clusters within the $Al_3(Sc,Ti)$ particle and the solute (Si, Mg, Cu, Zn, Mn) segregation at the surface of the $Al_3(Sc,Ti)$ particle.

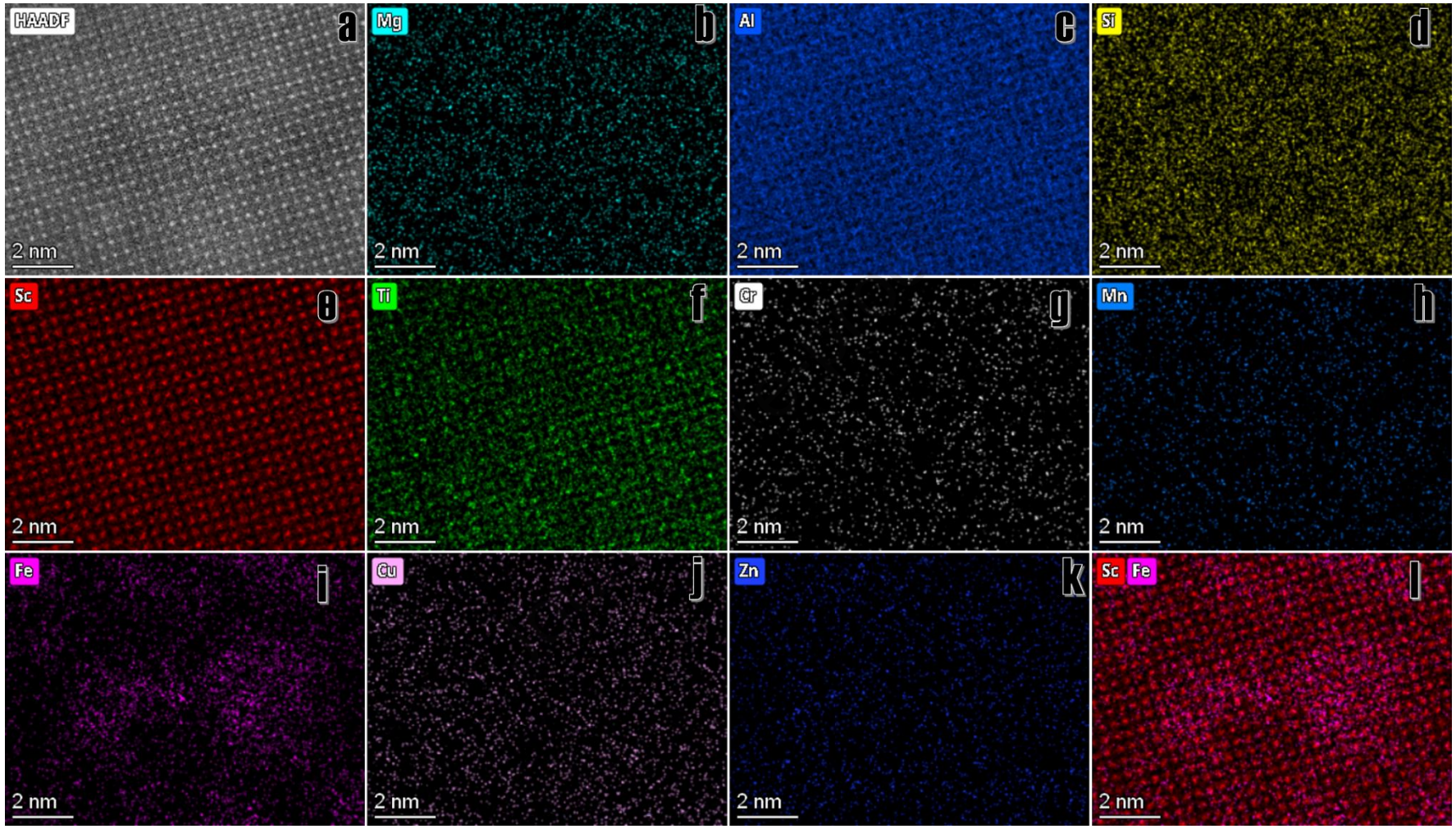


Figure 11. Atomic resolution STEM-EDS mapping demonstrates the Fe cluster within the $Al_3(Sc,Ti)$ particle and the Fe has no preferred atomic position within the particles which is different to the Ti which preferred at Sc atomic positions: (a) HAADF; (b) Mg; (c) Al; (d) Si; (e) Sc; (f) Ti; (g) Cr; (h) Mn; (i) Fe; (j) Cu; (k) Zn; (l) Sc and Fe.

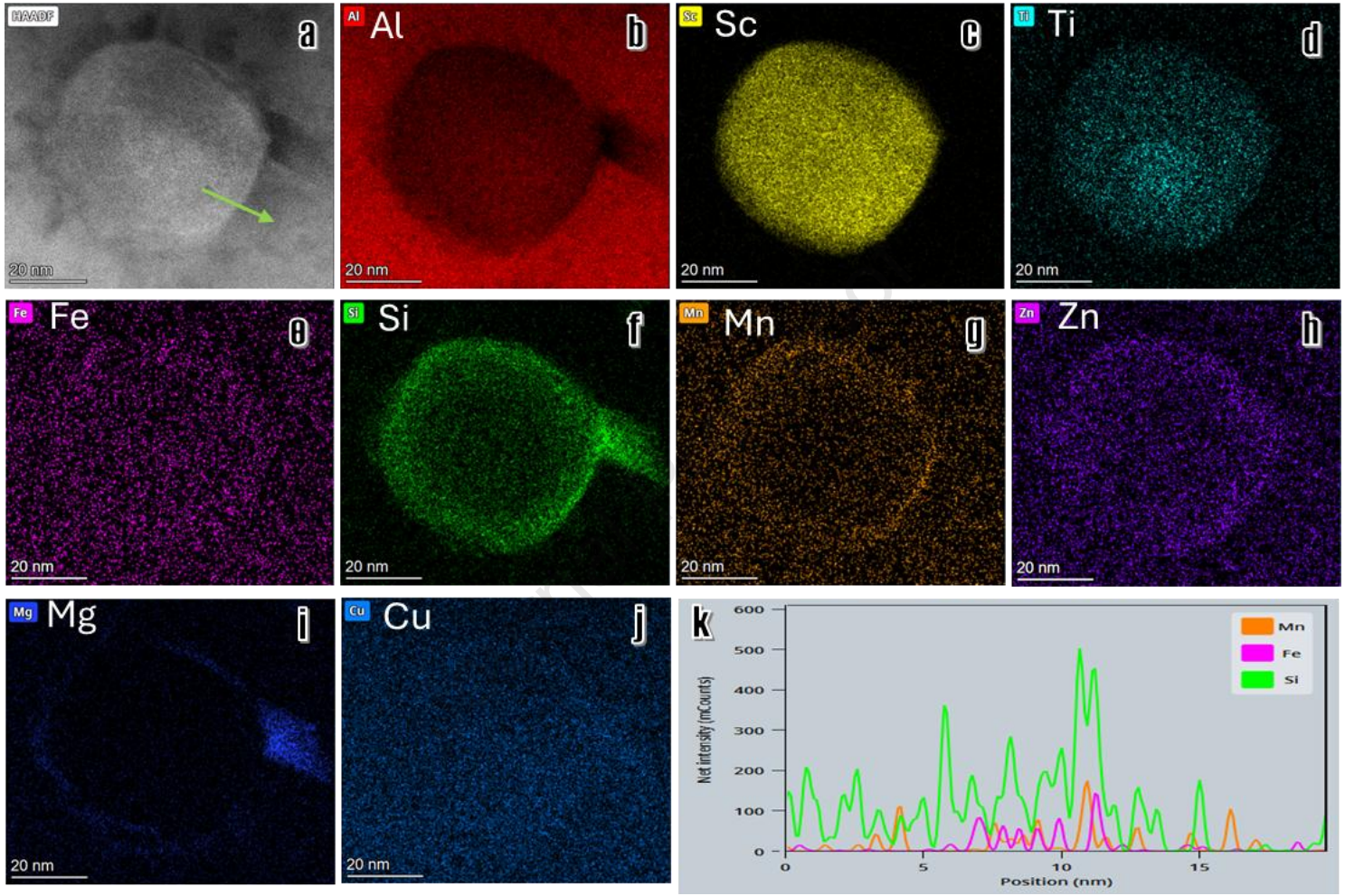


Figure 12. (a-k) STEM-EDS mapping showing the solute segregation after aging treatment (180 ºC x10 hrs) no more obvious Fe cluster within the $Al_3$(Sc,Ti) particle but more segregated at the surface of the particles where the other elements Si, Mn, Zn also segregate, Ti has some segregation within the particles rather than segregate to the surface; (k) the composition intensity of Mn, Fe, Si along the green arrow show in (a) presenting the segregation at the outer surface of particle.

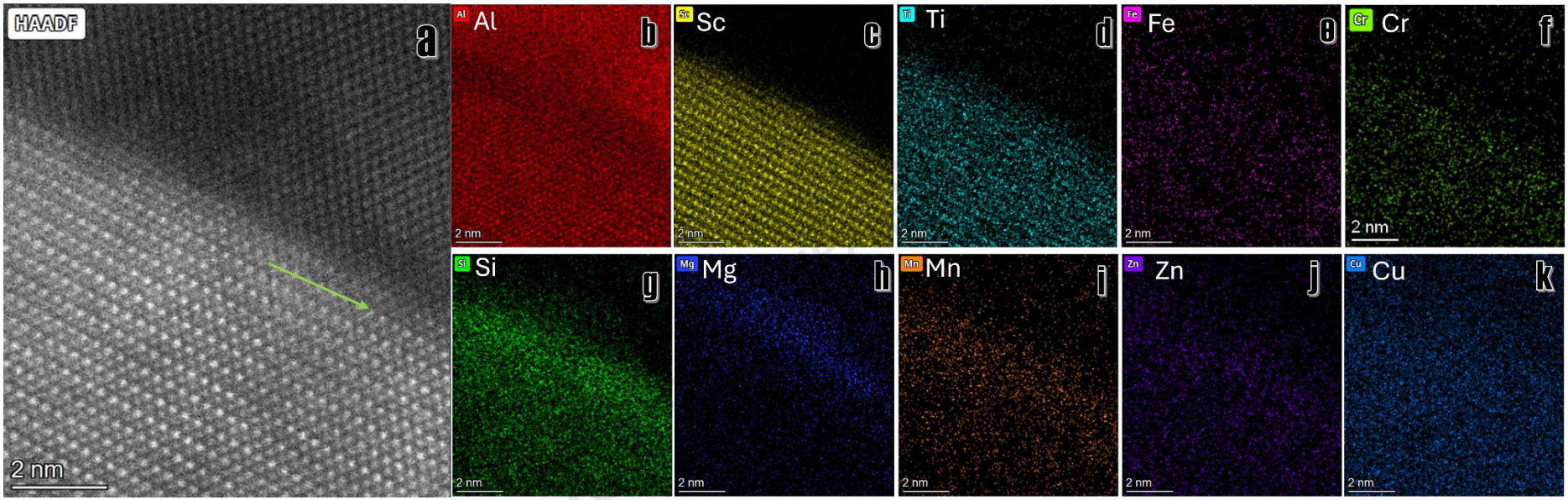


Figure 13. Atomic resolution STEM-EDS mapping showing the interface between the $Al_3$(Sc, Ti) precipitates and the Al matrix after heat treatment at 180 ºC for10 hrs: (a) HAADF image; (b) Al; (c) Sc; (d) Ti; (e) Fe; (f) Cr; (g) Si; (h) Mg; (i) Mn; (j) Zn; (k) Cu.

**Table 1** Composition of selected wrought Al grades from each series

| Element | 1*** 1050 | 2*** 2024 | 3*** 3003 | 4*** 4043 | 5*** 5052 | 6*** 6082 | 7*** 7075 |
|---|---|---|---|---|---|---|---|
| Al | 99.08 | 90.9 | 96.9 | 92.5 | 95.9 | 95.35 | 87.32 |
| Si | 0.25 | 0.5 | 0.6 | 6 | 0.25 | 1.3 | 0.4 |
| Mg | 0.05 | 1.8 | 0 | 0.2 | 2.8 | 1.2 | 2.9 |
| Cu | 0.05 | 4.9 | 0.2 | 0.3 | 0.1 | 0.1 | 2 |
| Zn | 0.07 | 0.25 | 0.1 | 0.1 | 0.1 | 0.2 | 6.1 |
| Fe | 0.4 | 0.5 | 0.7 | 0.6 | 0.4 | 0.5 | 0.5 |
| Mn | 0.05 | 0.9 | 1.5 | 0.15 | 0.1 | 1 | 0.3 |
| Cr | 0 | 0.1 | 0 | 0 | 0.35 | 0.25 | 0.28 |
| Ti | 0.05 | 0.15 | 0 | 0.15 | 0 | 0.1 | 0.2 |

**Table 2** Designed recycled wrought Al alloys based on calculated mixed recycled alloys compare to AA6082

| **wt.%** | **Al** | **Si** | **Mg** | **Cu** | **Zn** | **Fe** | **Mn** | **Cr** | **Ti** | **Total** |
|---|---|---|---|---|---|---|---|---|---|---|
| Nominated Recycled Alloy (RA) | Bal. | 1.33 | 1.28 | 1.09 | 0.99 | 0.51 | 0.57 | 0.14 | 0.09 | 6.0 |
| As-cast RA | Bal. | 1.34±0.035 | 1.31±0.05 | 1.09±0.03 | 1.00±0.03 | 0.56±0.014 | 0.58±0.01 | 0.13±0.002 | 0.09±0.003 | 6.1 |

**Table 3** STEM-EDS of the primary $Al_3(Sc,Ti)$ and precipitates $Al_3(Sc,Ti)$ particles with and without Fe clusters

| (wt.%) | Primary $Al_3Sc$ | Fe cluster area within $Al_3Sc$ precipitates | No Fe cluster area within $Al_3Sc$ precipitates | Average composition of $Al_3Sc$ precipitates |
|---|---|---|---|---|
| Samples | FIB | PIPS | PIPS | PIPS |
| Sc | 20.96±1.68 | 19.05±1.21 | 20.87±2.1 | 20.9±1.81 |
| Si | 0.87±0.19 | 2.88±0.56 | 2.67±0.45 | 2.4±0.52 |
| Ti | 5.13±0.57 | 1.73±0.04 | 1.42±0.06 | 2.01±0.12 |
| Mn | 0.07±0.02 | 0.32±0.03 | 0.46±0.03 | 0.33±0.02 |
| Fe | 0.09±0.02 | 3.8±0.41 | 0.36±0.02 | 0.63±0.02 |
| Cu | 4.24±0.45 | 1.09±0.03 | 1.38±0.04 | 1.28±0.04 |
| Zn | 0.54±0.04 | 1.00±0.04 | 1.08±0.04 | 1.17±0.05 |
| Cr | 0.05±0.02 | 0.77±0.04 | 0.14±0.03 | 0.36±0.04 |
| Mg | 0.07±0.02 | 0.83±0.03 | 1.07±0.04 | 0.52±0.03 |
| Total | 32 | 31.47 | 29.45 | 29.6 |

**Note:** The relatively high Cu content (in primary $Al_3Sc$) measured in the STEM-EDS analysis of the FIB-prepared TEM samples is attributed to the influence of the Cu sample grid material. In contrast, the PIPS-prepared samples did not exhibit this effect. However, due to the difficulty in preparing TEM samples containing primary $Al_3(Sc,Ti)$ particles, the FIB technique was necessary for sample preparation.

**Declaration of interests**

☒ The authors declare that they have no known competing financial interests or personal relationships that could have appeared to influence the work reported in this paper.

☐The authors declare the following financial interests/personal relationships which may be considered as potential competing interests: